Monthly Notices of the ROYAL ASTRONOMICAL SOCIETY

MNRAS **500,** 4042–4064 (2021) doi:10.1093/mnras/staa3116
Advance Access publication 2020 October 13

Abundance measurements of H_2O and carbon-bearing species in the atmosphere of WASP-127b confirm its supersolar metallicity

Jessica J. Spake [1,2,3★] David K. Sing,[1,2,4] Hannah R. Wakeford [5] Nikolay Nikolov,[6] Thomas Mikal-Evans [7] Drake Deming,[8] Joanna K. Barstow [9] David R. Anderson [10,11] Aarynn L. Carter [1] Michael Gillon,[12] Jayesh M. Goyal [13] Guillaume Hebrard,[14,15] Coel Hellier,[10] Tiffany Kataria,[16] Kristine W. F. Lam,[17] A. H. M. J. Triaud [18] and Peter J. Wheatley [11]

[1]*Physics and Astronomy, University of Exeter, Stocker Road, Exeter EX4 3RF, UK*
[2]*Department of Earth & Planetary Sciences, Johns Hopkins University, Baltimore, MD 21210, USA*
[3]*Division of Geological and Planetary Sciences, California Institute of Technology, 1200 East California Blvd, Pasadena, CA 91125, USA*
[4]*Department of Physics & Astronomy, Johns Hopkins University, Baltimore, MD 21210, USA*
[5]*School of Physics, HH Wills Physics Laboratory, University of Bristol, Tyndall Avenue, Bristol BS8 1TL, UK*
[6]*Space Telescope Science Institute, 3700 San Martin Dr, Baltimore, MD 21218, USA*
[7]*Kavli Institute for Astrophysics and Space Research, Massachusetts Institute of Technology, 77 Massachusetts Avenue, 37-241, Cambridge, MA 02139, USA*
[8]*Department of Astronomy, University of Maryland, College Park, MD 20742, USA*
[9]*School of Physical Sciences, The Open University, Walton Hall, Milton Keynes MK7 6AA, UK*
[10]*Astrophysics Group, Keele University, Staffordshire ST5 5BG, UK*
[11]*Department of Physics, University of Warwick, Gibbet Hill Road, Coventry CV4 7AL, UK*
[12]*Space sciences, Technologies and Astrophysics Research (STAR) Institute, Unieversite de Liege, 4031 Liege, Belgium*
[13]*Department of Astronomy and Carl Sagan Institute, Cornell University, 122 Sciences Drive, Ithaca, NY 14853, USA*
[14]*Sorbonne Universite, CNRS, UMR 7095, Institut d'Astrophysique de Paris, 98 bis bd Arago, F-75014 Paris, France*
[15]*Observatoire de Haute-Provence, CNRS, Universited Aix-Marseille, F-04870 Saint-Michel-l' Observatoire, France*
[16]*NASA Jet Propulsion Laboratory, 4800 Oak Grove Drive, Pasadena, CA 91109, USA*
[17]*Center for Astronomy and Astrophysics, Technical University Berlin, Hardenbergstr. 36, D-10623 Berlin, Germany*
[18]*School of Physics and Astronomy, University of Birmingham, Edgbaston, Birmingham B15 2TT, UK*

Accepted 2020 September 3. Received 2020 August 7; in original form 2019 November 19

ABSTRACT

The chemical abundances of exoplanet atmospheres may provide valuable information about the bulk compositions, formation pathways, and evolutionary histories of planets. Exoplanets with large, relatively cloud-free atmospheres, and which orbit bright stars provide the best opportunities for accurate abundance measurements. For this reason, we measured the transmission spectrum of the bright ($V \sim 10.2$), large ($1.37\,R_J$), sub-Saturn mass ($0.19\,M_J$) exoplanet WASP-127b across the near-UV to near-infrared wavelength range (0.3–5 μm), using the *Hubble* and *Spitzer Space Telescopes*. Our results show a feature-rich transmission spectrum, with absorption from Na, H_2O, and CO_2, and wavelength-dependent scattering from small-particle condensates. We ran two types of atmospheric retrieval models: one enforcing chemical equilibrium, and the other which fit the abundances freely. Our retrieved abundances at chemical equilibrium for Na, O, and C are all supersolar, with abundances relative to solar values of 9^{+15}_{-6}, 16^{+7}_{-5}, and 26^{+12}_{-9}, respectively. Despite giving conflicting C/O ratios, both retrievals gave supersolar CO_2 volume mixing ratios, which adds to the likelihood that WASP-127b's bulk metallicity is supersolar, since CO_2 abundance is highly sensitive to atmospheric metallicity. We detect water at a significance of 13.7σ. Our detection of Na is in agreement with previous ground-based detections, though we find a much lower abundance, and we also do not find evidence for Li or K despite increased sensitivity. In the future, spectroscopy with *James Webb Space Telescope* will be able to constrain WASP-127b's C/O ratio, and may reveal the formation history of this metal-enriched, highly observable exoplanet.

Key words: techniques: spectroscopic – planets and satellites: atmospheres – stars: individual: WASP-127.

1 INTRODUCTION

WASP-127b is a transiting, sub-Saturn mass exoplanet that was discovered by the SuperWASP survey (Lam et al. 2017). It has the largest expected atmospheric scale height of any planet yet discovered, at ∼2350 km. Its host star is bright ($V \sim 10.2$, $J \sim 9.1$), and appears to be old, photometrically quiet, and slowly rotating.[1] These planetary and stellar properties make WASP-127b a standout target for atmospheric characterization, because they result in large

[1]WASP-127's age estimate from isochrone fitting is 11.41 ± 1.80 Gyr; the SuperWASP photometry shows no sign of variability; and the stellar $v \sin i$ value is too small to measure from high-resolution spectra (Lam et al. 2017).

★ E-mail: jessica.spake@gmail.com

transmission signals that are not affected by stellar variability. With the Hubble (*HST*) and *Spitzer Space Telescopes*, it is possible to measure a transmission spectrum rivalling the quality of even the canonical planets HD 209458b and HD 189733b (Charbonneau et al. 2002; Sing et al. 2011; Deming et al. 2013; Pont et al. 2013). Importantly, with a mass of only 0.19 M_J, WASP-127b is the most observationally accessible low-mass, gas-giant exoplanet. Evidence of sodium, lithium, and potassium at supersolar abundances has been reported by Palle et al. (2017), Chen et al. (2018), and Žák et al. (2019), using the ground-based NOT, GTC, and HARPS telescopes, respectively. Palle et al. (2017) also report an intriguingly sharp rise in WASP-127b's transmission spectrum shortwards of 0.4 μm, measured with NOT, which they attribute to a mystery UV absorber. While this paper was under review, Skaf et al. (2020) reported an independent analysis of the same *HST* near-infrared spectroscopic data presented here, and measured a supersolar water abundance in WASP-127b's atmosphere.

In this work, we present new transit observations of WASP-127b from the *Hubble Space Telescope* and *Spitzer Space Telescope*. We carried out the joint *HST* and *Spitzer* programme to observe a broad optical-to-infrared transmission spectrum for WASP-127b. The combined wavelength coverage of the programme from 0.3 to 5 μm covers strong expected molecular absorption features from water and carbon-bearing species in the infrared, along with sodium and potassium absorption features, and Rayleigh scattering caused by high-altitude aerosols and H_2 in the optical region. With this study, we aimed to classify WASP-127b as cloudy or cloud-free, and measure the abundances of important gaseous species such as H_2O, Na, and K. Our analysis confirms the supersolar abundances for WASP-127b, and we additionally find new evidence of absorption from carbon-bearing species and strong evidence that submicron-sized particles are responsible for wavelength-dependent opacity from 0.3 to 1.6 μm (instead of a wavelength-independent absorber). In the future, WASP-127b will likely become a focus of intensive *James Webb Space Telescope* (*JWST*) observations. The characterization described here will allow the community to optimize scientific objectives, instrument set-up, and phase coverage for these future *JWST* observations.

We describe the observations and data reductions in Section 2, discuss the transit light-curve fitting in Section 3, present atmospheric retrievals in Section 4, and conclude with the results and discussion in Section 5.

2 OBSERVATIONS AND DATA REDUCTION

The *HST* and *Spitzer Space Telescope* observations were made as part of a joint *HST*/Spitzer programme GO:14619 (PI: Spake). We observed five transits of WASP-127b using different instrument set-ups with *HST* and *Spitzer*, in order to build a transmission spectrum covering the 0.3–5 μm wavelength range. In addition, the *Transiting Exoplanet Survey Satellite* (*TESS*) observed four photometric transits of WASP-127b in Sector 9. A summary of the observations is given in Table 1.

Table 1. Summary of transit observations of WASP-127b.

Instrument	Start date (UTC)	Wavelength range (Å)	Duration (h)
HST/STIS + G430L	2018-06-23	2900–5700	6.8
HST/STIS + G750L	2018-02-18	5240–10 270	6.8
HST/WFC3 + G141	2018-04-09	11 000–17 000	6.8
Spitzer/IRAC Ch1	2017-04-02	31 750–39 250	9
Spitzer/IRAC Ch2	2017-04-06	39 850–50 050	9
TESS	2019-03-05	6000–10 000	9
TESS	2019-03-09	6000–10 000	9
TESS	2019-03-18	6000–10 000	9
TESS	2019-03-22	6000–00	9

2.1 TESS

TESS (Ricker et al. 2015) provides time-series photometry in a bandpass covering 0.6–1.0 μm, and it observed four transits of WASP-127b in 2019 March (Sector 9) at 2-min cadence. The high-cadence and multiple, opportunistic transit observations meant we could use the *TESS* data to refine the transit ephemeris and physical parameters of the WASP-127 system. This was particularly useful since our *HST* observations do not cover much of the ingress or egress of WASP-127b's transit. We used the *TESS* presearch data conditioning (PDC) light curve of WASP-127b (Fig. A1), which has been corrected for effects such as non-astrophysical variability and crowding (Jenkins et al. 2016). We removed all photometric points that were flagged with anomalies, and converted the Barycentric TESS Julian Dates (BTJD) to BJD_{TDB} by adding 2457 000 d. For each of the four transits, we extracted the data in a 0.5 d window centred around the mid-transit time, and fit each transit event individually.

2.2 Spitzer/IRAC

We observed WASP-127b during two primary transits using the subarray mode with *Spitzer*/IRAC channels 1 and 2, using 2 s integration times, for 9 h each visit, with the duration set to include the 3.5 h transit and a baseline equally as long to precisely measure the transit depth (plus some extra time as insurance). WASP-127's expected flux is 75/52 mJy for 3.6/4.5 μm, and our 2 s exposure time was short enough to stay well below saturation. The subarray mode allowed for high-cadence observations that aid in removing the detector intrapixel sensitivity, and reduce data storage overheads. Each visit could only be done at a single wavelength requiring two transits to observe at 3.6 and 4.5 μm, as cycling between the two channels greatly exacerbates the intrapixel sensitivity noise. Each observation began with a recommended Pointing Calibration and Reference Sensor peak-up mode of 30 min, which locates the star into the subarray pixel 'sweet spot' and helps mitigate the intrapixel sensitivity effects providing <100 parts per million (ppm) accuracies.

For both *Spitzer* channels, we followed the data reduction and photometry procedures of Evans et al. (2015). We reduced the basic calibrated data (BCD) frames for each light curve using a publicly available PYTHON pipeline,[2] which does the following: first, it calculates the background level and locates the stellar centroid in each BCD frame. It estimates the background from the median pixel value of four 8×8 pixel subarrays at the corners of each frame, and then subtracts that value from each pixel in the array. It finds the centroid coordinates by taking the flux-weighted mean of a 7×7 pixel subarray centred on the star. The pipeline computes exposure mid-times in Barycentric Julian Date Coordinated Universal Time (BJD_{UTC}) using the $BMJD_{OBS}$ and *FRAMTIME* header entries. It flags bad frames by identifying frames whose centroid coordinates or pixel counts deviate by 5σ from those of the 30 frames immediately preceding and following each frame. We removed bad frames from the analysis. We iterated this bad-frame identification twice, and discarded less than 5 per cent of the frames.

[2]from www.github.com/tomevans.

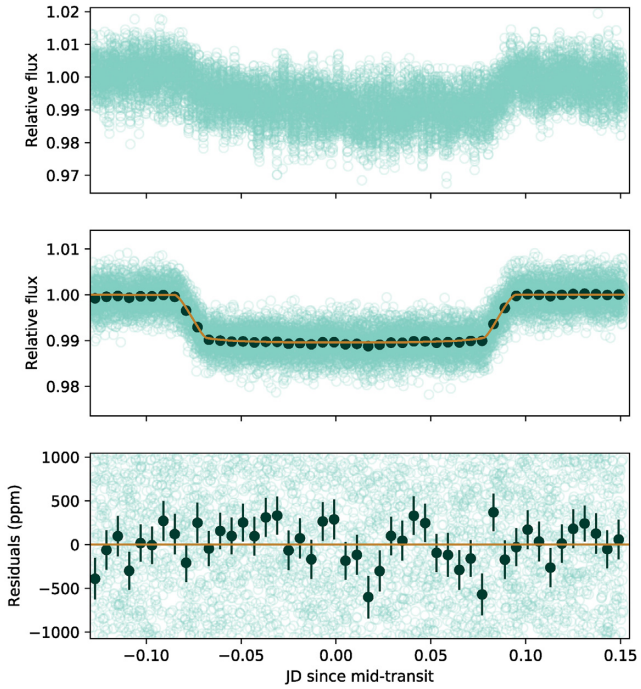

Figure 1. Light-curve fit for WASP-127b using *Spitzer*/IRAC's 3.6 μm channel. Top panel: Light green points are raw data. Middle panel: Light green points are data divided by systematics model, black points are data in 9 min bins for clarity, beige curve is the best-fitting transit model. Bottom panel: Best-fitting model residuals.

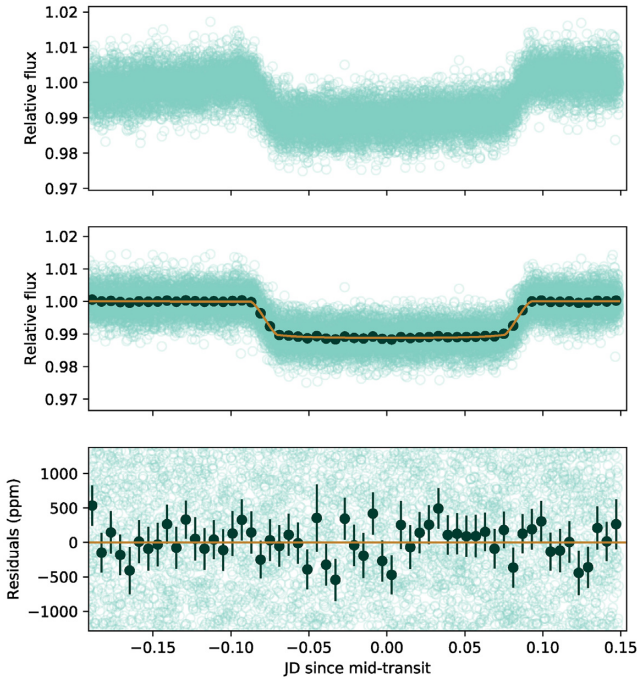

Figure 2. Light-curve fit for WASP-127b using *Spitzer*/IRAC's 4.5 μm channel. Top panel: Light green points are raw data. Middle panel: Light green points are data divided by systematics model, black points are data in 9 min bins for clarity, beige curve is the best-fitting transit model. Bottom panel: Best-fitting model residuals.

The pipeline performed photometry on each remaining frame by summing the pixel counts within circular apertures of various sizes between 1.5 and 6 pixels, in increments of 0.5 pixels. Because the IRAC point spread function (PSF) is undersampled, we linearly interpolated the pixel array on to a 10 × 10 supersampled grid, which has previously been done by Stevenson et al. (2010), for example. We counted the interpolated subpixels towards the aperture sum if their centres fell within the aperture radius. Our selected photometric light curves are shown in Figs 1 and 2, and we discuss how the apertures were chosen in Section 3.2.

2.3 STIS

We observed two transits with *HST*'s Space Telescope Imaging Spectrograph (STIS), one each with the G430L and G750L gratings. We followed an observing strategy proven to produce high signal-to-noise spectra (e.g. Brown et al. 2001, Sing et al. 2011, Huitson et al. 2012, Nikolov et al. 2015). The data were taken on 2018-06-23 and 2018-02-18, covering wavelengths of 2900–5700 and 5240–10 270 Å, respectively. Visits 1 and 2 both lasted 4.5 spacecraft orbits each. One *HST* orbit lasts ∼96 min during which WASP-127b is visible for ∼45 min, leaving ∼45 min gaps in the data as the spacecraft passes through the Earth's shadow. WASP-127b has a long transit duration (∼3.5 h, compared to ∼2 h for a typical hot Jupiter, e.g. HD 209458b). We scheduled each visit such that two orbits fell fully inside a transit and 1.5 fell either side of it, in order to accurately measure the baseline stellar flux. We used integration times of 280 and 180 s, resulting in a total of 48 and 58 low-resolution spectra ($\Delta\lambda/\lambda = 500$) for the G430L and G750L visits, respectively. We used 52 arcsec × 2 arcsec slits to minimize slit losses, and minimized the data-acquisition overheads by reading out a smaller portion of the CCD (128 × 128 pixels).

Our data reduction method for STIS follows previous works such as Sing et al. (2013), Huitson et al. (2013), and Nikolov et al. (2014, 2015). We used the most recent version of the CALSTIS automatic reduction pipeline (Katsanis & McGrath 1998) included in IRAF[3] (Tody 1993) to reduce the raw STIS data (which involves bias-, dark-, and flat-correction). Similarly to Nikolov et al. (2015), we corrected the G750L spectra for fringing effects with the method described in Goudfrooij & Christensen (1998). Further, we used the method described in Nikolov et al. (2013) to correct the data for cosmic rays and bad pixels flagged by the CALSTIS pipeline. We then extracted 1D spectra from the reduced data frames using IRAF's APALL. We used aperture widths ranging from 3.5 to 10.5 pixels, in 1-pixel steps, and found the aperture width for each visit that gave the lowest residual scatter in the white light curve (see Section 3.4.2). The selected aperture widths were 9.5 and 10.5 pixels for G430L and G750L, respectively. Finally, the wavelength solutions for each spectrum were obtained from the *x1d* files from CALSTIS, and the spectra were then cross-correlated with the median of the out-of-transit spectra to place them on a common wavelength scale, which helps to account for subpixel shifts in the dispersal direction.

2.4 WFC3

We observed one spectroscopic transit of WASP-127b using *HST*'s Wide Field Camera 3 (WFC3) instrument with the infrared G141

[3]IRAF is distributed by the National Optical Astronomy Observatories, which are operated by the Association of Universities for Research in Astronomy, Inc., under cooperative agreement with the National Science Foundation.

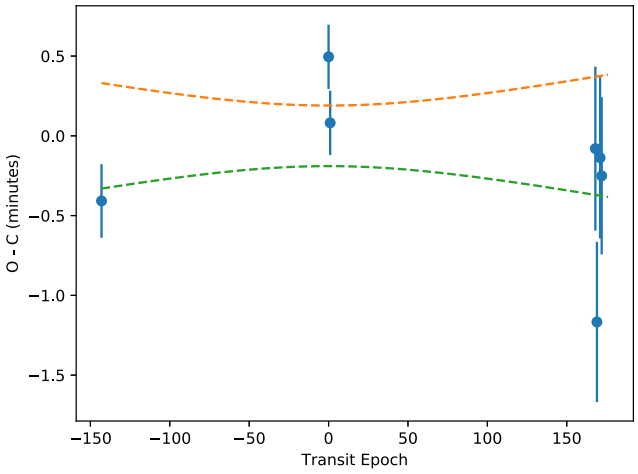

Figure 3. Timing offsets from the fitted mid-transit times for WASP-127b. Label discovery paper, *TESS*, and *Spitzer* data. Transit epoch centred on *Spitzer* data.

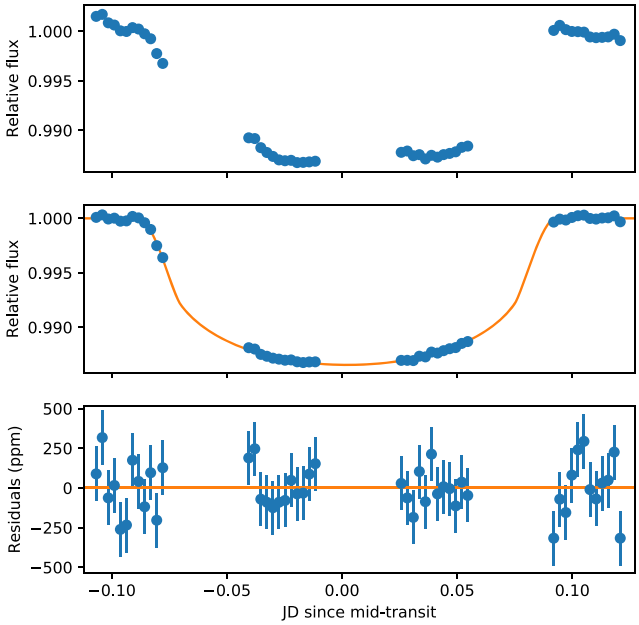

Figure 4. White light-curve fit for WASP-127b using *HST*/STIS + G430L, covering the entire 2900–5700 Å wavelength range. Top panel: Raw flux before detrending, divided by the median of the out-of-transit data. Middle panel: Points are data divided by systematics model, curve is the best-fitting transit model. Bottom panel: Best-fitting model residuals.

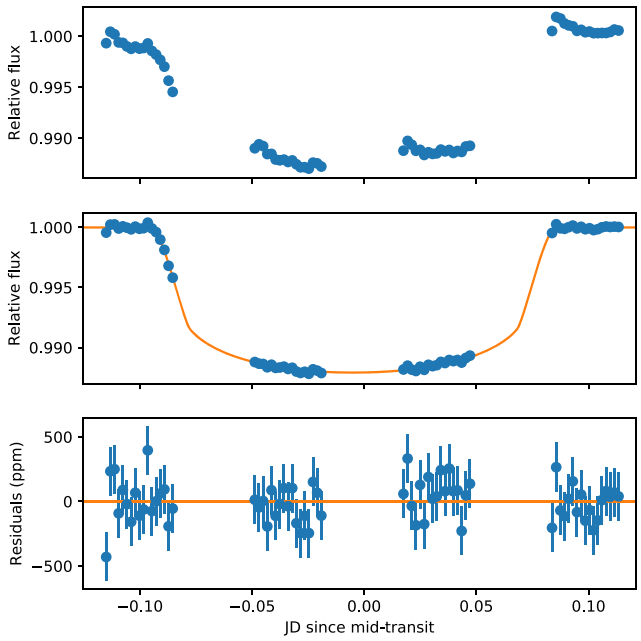

Figure 5. White light-curve fit for WASP-127b using *HST*/STIS + G750L, covering the entire 5240–10 270 Å wavelength range. Top panel: Raw flux before detrending, divided by the median of the out-of-transit data. Middle panel: Points are data divided by systematics model, curve is the best-fitting transit model. Bottom panel: Best-fitting model residuals.

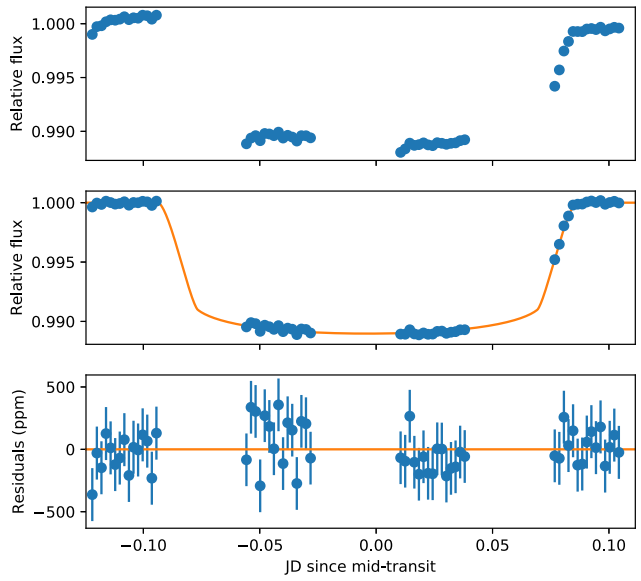

Figure 6. White light-curve fit for WASP-127b using *HST*/WFC3 + G141, covering the entire 11 000–17 000 Å wavelength range. Top panel: Raw flux before detrending, divided by the median of the out-of-transit data. Middle panel: Points are data divided by systematics model, curve is the best-fitting transit model. Bottom panel: Best-fitting model residuals.

grism. The observations spanned the approximate wavelength range of 11 000–17 000 Å, which covered a broad-band of water absorption lines centred on 14 000 Å. We used *HST*'s spatial scan mode and a scan rate of 1 pixel per second for 15 observations of 120 s each, which spread WASP-127's spectrum over 120 pixels. We used the SPARS10 sampling sequence with 14 non-destructive reads per exposure (NSAMP = 14). The maximum number of electron counts per pixel was 29 000 – which is approximately 40 per cent of the saturation limit of the detector. The raw frames were first reduced with the automatic pipeline. The 1D spectra were then extracted following standard methods (e.g. Evans et al. 2017), i.e. by building up flux counts by summing the difference between successive non-destructive reads. First, we removed the background from each read difference by subtracting the median of a box of pixels uncontaminated by the spectrum. Then, we found the flux-weighted centre of each read difference and set to zero all pixels more than 70 rows away from the centre in the cross-dispersion axis, which removes a majority of the cosmic rays. The remaining cosmic rays were flagged by finding 4σ outliers relative to the median along

Table 2. Results from light-curve fit for WASP-127b using *Spitzer*/IRAC Channel 1 (3.6 μm) and Channel 2 (4.5 μm).

Parameter	Value	
Period (d)	4.178^{a}	
a/R_*	8.044^{a}	
Inclination (°)	88.7^{b}	
Eccentricity	0^{b}	
Arg. of periastron	90^{b}	
	Channel 1	Channel 2
Transit depth (per cent)	$0.993^{+0.005}_{-0.005}$	$1.073^{+0.006}_{-0.006}$
Mid-time (JD)	$2\,457\,846.19996^{+0.00004}_{-0.00003}$	$2\,457\,850.37968^{+0.00001}_{-0.00001}$
LD coefficients ($u_{1,2}$)	0.0626^{c}, 0.1734^{c}	0.0639^{c}, 0.1374^{c}

Note.[a]Period and transit mid-times fixed to values found from our updated fit described in Section 3.3.
[b]Planet parameters fixed to values from Lam et al. (2017).
[c]Limb darkening parameters fixed from ATLAS models (Castelli & Kurucz 2004).

the dispersion direction. We replaced each flagged pixel with the median along the dispersion direction, rescaled to the count rate of the cross-dispersion column. We then summed the corrected read differences to produce background- and cosmic ray-corrected 2D images of the spatially scanned spectrum. We extracted 1D spectra from the corrected images by summing the flux in a rectangular aperture, centred on the flux-weighted centre of the scan. The aperture spanned the full dispersion axis and was 140 pixels wide in the spatial direction.

We found the wavelength solutions by cross-correlating the extracted spectra with an ATLAS model stellar spectrum (Castelli & Kurucz 2004) which most closely matches WASP-127 ($T_{\rm eff}$ = 5500 K, log g = 4.0 cgs); modulated by the G141 grism throughput. Following standard methods (Kreidberg et al. 2018), we interpolated each spectrum on to the wavelength range of the first to account for shifts in the dispersion axis over time.

3 LIGHT-CURVE FITTING

3.1 TESS

We fit each of the four *TESS* transit light curves separately, using the four-parameter, non-linear, limb-darkened transit model of Mandel & Agol (2002), multiplied by a linear baseline time trend. We used the method of Sing (2010) to estimate the limb-darkening coefficients, using the ATLAS model stellar spectrum (Castelli & Kurucz 2004) which most closely matched WASP-127b ($T_{\rm eff}$ = 5500 K, log g = 4.0 cgs). We found limb-darkening coefficients of c_1 = 0.5802, c_2 = −0.1496, c_3 = 0.5504, and c_4 = −0.3115.

For each of the four transits, we fit for six free parameters: the central transit time; planet-to-star radius ratio ($R_{\rm P}/R_*$); two coefficients for the linear baseline; the cosine of the orbital inclination (i); and a/R_* (where a is the semimajor axis and R_* the stellar radius). We found weighted-average parameter values, including the radius ratio of $R_{\rm P}/R_*$ = 0.10060 ± 0.00038; orbital inclination of i = 87.6 ± 1.0 deg; and a/R_* = 7.83 ± 0.30. The inclination and a/R_* were used as fixed values in the *HST* and *Spitzer* analyses. We found the four transit mid-times to be 2458548.120564 ± 0.000357, 2458552.297877 ± 0.000349, 2458560.654727 ± 0.000351, and 2458564.832716 ± 0.000342, in BDJ$_{\rm TBD}$. The four individually measured radius ratios were 0.10105 ± 0.00109, 0.10088 ± 0.00105, 0.10067 ± 0.00111, and 0.10043 ± 0.00049. The lack of variation in both the radius ratio and the observed stellar flux over the *TESS* observational period (Figs A1 and A2) increases the evidence that WASP-127 is a photometrically quiet star. Therefore, we should not expect stellar activity to vary the transit depths measured at different epochs.

3.2 Spitzer

We used the same light-curve fitting procedure for both *Spitzer*/IRAC channels. *Spitzer* photometry is prone to large intrapixel systematics (e.g. Deming et al. 2005). To correct for this, we fit for a two-dimensional quadratic trend in the photometry with the x and y position of WASP-127's centroid (measured using the pipeline discussed in Section 2.2). The function has the form

$$F = c_{2,\rm x}x^2 + c_{2,\rm y}y^2 + c_{1,\rm x}x + c_{1,\rm y}y + c_{\rm xy}xy, \quad (1)$$

and we fit for the following five free parameters: $c_{2,\rm x}$, $c_{1,\rm x}$, $c_{2,\rm y}$, $c_{1,\rm y}$, and $c_{\rm x,y}$. We used the BATMAN PYTHON package (Kreidberg 2015) to model the transit light-curve signal, and fit for the planet-to-star radius ratio ($R_{\rm p}/R_*$) and mid-transit time (t_0). We also fit for the gradient (c_1) and linear trend (c_0) in the baseline in the photometry. In total, there were nine free parameters in the light-curve fit. We used the Markov chain Monte Carlo (MCMC) package EMCEE (Foreman-

Table 3. Fixed planet parameters and results from white light-curve fits for WASP-127b using *HST*.

Parameter	Value		
a/R_*	8.044^{a}		
Inclination (°)	88.7^{a}		
Eccentricity	0^{a}		
Arg. of periastron	90^{a}		
Period (d)	4.178^{b}		
	STIS + G430L	STIS + G750L	WFC3 + G141
Transit depth (per cent)	$1.034^{+0.006}_{-0.005}$	$1.013^{+0.009}_{-0.006}$	$0.996^{+0.011}_{-0.011}$
Mid-time (JD)	$2\,458\,293.2528^{b}$	$2\,458\,293.2528^{b}$	$2\,458\,293.2528^{b}$
u_1	0.5466^{c}	0.7017^{c}	0.5944^{c}
u_2	-0.3781^{c}	-0.5462^{c}	0.0707^{c}
u_3	1.2964^{c}	1.1008^{c}	-0.1204^{c}
u_4	-0.5955^{c}	-0.5233^{c}	0.0202^{c}

Note.[a]Planet parameters fixed to values from (Lam et al. 2017).
[b]Period and transit mid-times fixed to values found from our updated fit described in Section 3.3.
[c]Limb darkening parameters fixed from ATLAS models (Castelli & Kurucz 2004).

Table 4. Results from spectroscopic light-curve fits for WASP-127b, using *HST*/STIS + G430L. Fixed, four-parameter limb darkening law coefficients denoted by u_i.

Bin start (Å)	Bin end (Å)	Transit depth (per cent)	u_1	u_2	u_3	u_4
2898	3700	$1.050^{+0.037}_{-0.044}$	0.5188	− 0.8368	2.0778	− 0.815
3700	4041	$1.048^{+0.018}_{-0.021}$	0.7102	− 1.1242	2.1235	− 0.7717
4041	4261	$1.027^{+0.014}_{-0.015}$	0.5224	− 0.6401	1.7752	− 0.738
4261	4426	$1.028^{+0.014}_{-0.013}$	0.6179	− 0.7511	1.7207	− 0.6878
4426	4536	$1.025^{+0.009}_{-0.012}$	0.4502	− 0.2005	1.2133	− 0.5686
4536	4646	$1.035^{+0.016}_{-0.018}$	0.4359	− 0.1007	1.0827	− 0.531
4646	4756	$1.013^{+0.015}_{-0.013}$	0.4582	− 0.146	1.1212	− 0.5536
4756	4921	$1.023^{+0.011}_{-0.011}$	0.4853	− 0.143	1.0708	− 0.5453
4921	5030	$1.028^{+0.012}_{-0.012}$	0.519	− 0.2152	1.0986	− 0.5414
5030	5140	$1.034^{+0.016}_{-0.015}$	0.5397	− 0.2945	1.1957	− 0.5839
5140	5250	$1.005^{+0.014}_{-0.012}$	0.6078	− 0.465	1.3201	− 0.616
5250	5360	$1.024^{+0.019}_{-0.014}$	0.5829	− 0.3203	1.1244	− 0.5466
5360	5469	$1.024^{+0.019}_{-0.016}$	0.575	− 0.2891	1.0862	− 0.5385
5469	5579	$1.007^{+0.016}_{-0.017}$	0.5927	− 0.3243	1.1044	− 0.5449
5579	5688	$1.036^{+0.014}_{-0.015}$	0.6041	− 0.3355	1.09	− 0.5378

Table 5. Results from spectroscopic light-curve fits for WASP-127b, using *HST*/STIS + G750L. Fixed, four-parameter limb darkening law coefficients denoted by u_i.

Bin start (Å)	Bin end (Å)	Transit depth (per cent)	u_1	u_2	u_3	u_4
5500	5600	$1.023^{+0.027}_{-0.021}$	0.5963	− 0.3281	1.1005	− 0.5429
5600	5700	$1.047^{+0.022}_{-0.023}$	0.6029	− 0.3282	1.0782	− 0.5331
5700	5800	$1.014^{+0.014}_{-0.014}$	0.5987	− 0.2994	1.0337	− 0.5182
5800	5878	$1.051^{+0.018}_{-0.020}$	0.593	− 0.2704	0.9903	− 0.5042
5878	5913	$1.066^{+0.024}_{-0.023}$	0.6326	− 0.3954	1.1143	− 0.5468
5913	6070	$1.026^{+0.014}_{-0.017}$	0.6126	− 0.3129	1.0114	− 0.5113
6070	6200	$1.028^{+0.020}_{-0.016}$	0.6537	− 0.4235	1.0947	− 0.5342
6200	6300	$1.022^{+0.018}_{-0.020}$	0.6632	− 0.4382	1.094	− 0.5331
6300	6450	$1.036^{+0.015}_{-0.016}$	0.6696	− 0.455	1.0978	− 0.5349
6450	6600	$0.995^{+0.020}_{-0.017}$	0.6986	− 0.4715	1.0601	− 0.5246
6600	6800	$1.004^{+0.013}_{-0.012}$	0.6883	− 0.5005	1.1059	− 0.5346
6800	7000	$0.997^{+0.016}_{-0.012}$	0.7015	− 0.5355	1.1128	− 0.5306
7000	7200	$1.009^{+0.013}_{-0.014}$	0.732	− 0.6214	1.1791	− 0.551
7200	7450	$1.018^{+0.011}_{-0.011}$	0.7449	− 0.658	1.1933	− 0.5537
7450	7645	$1.003^{+0.017}_{-0.016}$	0.7339	− 0.6262	1.1383	− 0.5317
7645	7720	$1.020^{+0.022}_{-0.026}$	0.7356	− 0.6251	1.115	− 0.5196
7720	8100	$1.010^{+0.020}_{-0.019}$	0.749	− 0.6699	1.1521	− 0.5322
8100	8485	$0.986^{+0.026}_{-0.018}$	0.7713	− 0.7465	1.2143	− 0.555
8485	8985	$1.005^{+0.023}_{-0.018}$	0.7557	− 0.7033	1.1225	− 0.5143
8985	10240	$1.025^{+0.018}_{-0.017}$	0.7199	− 0.6086	0.9678	− 0.4452

Mackey et al. 2013) to marginalize over the parameter space of the model likelihood distribution. We used 100 walkers and ran chains for 5000 steps, discarding the first 1000 as burn-in before combining the walker chains into a single chain. We followed this procedure for each of the photometric light curves that we produced, which used varying aperture sizes from a radius of 1.5–6 pixels, in increments of 0.5 pixels. Here, we quote the results from the light curve which had the lowest model residuals after the fitting process. For the 3.6 μm channel, the optimum aperture radius was 3.0 pixels, and for the 4.5 μm channel it was 2.5 pixels. Table 2shows our best-fitting transit depths and mid-transit times for each channel. Figs 1 and 2 show the light curves with their best-fitting models and residuals, and Figs B1 and B2 show the posterior distributions of these fits.

Our results were consistent with those inferred by a more sophisticated treatment of *Spitzer*'s systematics. Deming et al. (2015) use a technique that involves modelling the light curves of individual pixels to correct for *Spitzer*'s intrapixel variations, called pixel level decorrelation (PLD). The measured transit depths using both PLD and the light-curve fitting procedure described above are shown in Fig. 18. For both channels they are consistent within 1σ.

3.3 Period and ephemeris fitting

WASP-127b has a long, ∼3 h transit, which, combined with the Earth occultations occurring in each *HST* orbit, meant we are unable to get continuous phase coverage of the target over the full transit. Because of the particular timings of our observations, we did not observe much of the ingress or the egress on any of the three *HST* transit observations. This made it difficult to fit for the transit mid-time. Indeed, when we did fit for the transit mid-time our best-fitting solution for the WFC3 visit was earlier than expected by 6 min.

Table 6. Results from spectroscopic light-curve fits for WASP-127b, using *HST*/WFC3 + G141. Fixed, four-parameter limb darkening law coefficients denoted by u_i.

Bin start (Å)	Bin end (Å)	Transit depth (per cent)	u_1	u_2	u_3	u_4
11 225	11 409	$0.993^{+0.009}_{-0.009}$	0.6515	− 0.4064	0.6627	− 0.3206
11 409	11 594	$0.995^{+0.008}_{-0.007}$	0.6312	− 0.3375	0.5764	− 0.2851
11 594	11 779	$1.001^{+0.009}_{-0.010}$	0.6281	− 0.3166	0.544	− 0.2745
11 779	11 963	$0.991^{+0.010}_{-0.009}$	0.6205	− 0.287	0.5009	− 0.2564
11 963	12 148	$1.001^{+0.008}_{-0.009}$	0.6093	− 0.2483	0.4502	− 0.2362
12 148	12 333	$0.991^{+0.008}_{-0.008}$	0.5884	− 0.162	0.3459	− 0.1968
12 333	12 517	$0.992^{+0.008}_{-0.007}$	0.5787	− 0.1206	0.2867	− 0.1716
12 517	12 702	$1.000^{+0.012}_{-0.011}$	0.5727	− 0.0874	0.2388	− 0.1533
12 702	12 887	$0.993^{+0.008}_{-0.008}$	0.5709	− 0.0386	0.1613	− 0.1299
12 887	13 071	$0.997^{+0.009}_{-0.009}$	0.554	0.006	0.1075	− 0.0997
13 071	13 256	$1.010^{+0.007}_{-0.008}$	0.5476	0.0484	0.0384	− 0.0685
13 256	13 441	$1.016^{+0.008}_{-0.008}$	0.5386	0.1046	− 0.0462	− 0.0321
13 441	13 625	$1.054^{+0.009}_{-0.010}$	0.5338	0.1452	− 0.1094	− 0.0057
13 625	13 810	$1.051^{+0.011}_{-0.011}$	0.5332	0.1813	− 0.1788	0.0266
13 810	13 995	$1.052^{+0.008}_{-0.008}$	0.5265	0.2444	− 0.2789	0.0708
13 995	14 179	$1.046^{+0.007}_{-0.007}$	0.5238	0.2836	− 0.3521	0.1059
14 179	14 364	$1.053^{+0.007}_{-0.006}$	0.5301	0.2999	− 0.4012	0.1308
14 364	14 549	$1.046^{+0.010}_{-0.011}$	0.5418	0.3015	− 0.431	0.1464
14 549	14 733	$1.042^{+0.009}_{-0.009}$	0.5518	0.3122	− 0.4668	0.1632
14 733	14 918	$1.031^{+0.009}_{-0.010}$	0.567	0.29	− 0.4699	0.1709
14 918	15 102	$1.028^{+0.009}_{-0.012}$	0.5795	0.2891	− 0.5072	0.1952
15 102	15 287	$1.012^{+0.010}_{-0.010}$	0.5983	0.31	− 0.585	0.2369
15 287	15 472	$0.999^{+0.010}_{-0.009}$	0.631	0.2627	− 0.5741	0.2409
15 472	15 656	$1.001^{+0.010}_{-0.011}$	0.6489	0.2307	− 0.5607	0.2408
15 656	15 841	$0.983^{+0.009}_{-0.009}$	0.6836	0.13	− 0.4668	0.2097
15 841	16 026	$0.986^{+0.009}_{-0.009}$	0.7076	0.0634	− 0.4054	0.19
16 026	16 210	$0.975^{+0.012}_{-0.011}$	0.7347	0.0371	− 0.4274	0.21
16 210	16 395	$0.967^{+0.013}_{-0.012}$	0.7468	0.0085	− 0.4018	0.2017

Large inaccuracies in the mid-transit time can change the measured transit depth. However, the *TESS* and *Spitzer* observations have high cadence and full phase coverage, and so their mid-transit times may be more reliable. They can also be used to update the discovery-paper period and ephemeris so that the mid-transit times for the *HST* visits can be fixed to more reliable values. We fit the discovery paper reported values, all four *TESS* transit times, and two *Spitzer* transit times with a linear trend in time, fitting for the period and ephemeris (Fig. 3). Our best-fitting period was 4.17807 ± 0.00013 d, and our best-fitting ephemeris was 2457846.20526 ± 0.00013. The updated period and ephemeris were used to fix the mid-transit times for all three *HST* transit observations.

3.4 HST: STIS and WFC3

We followed the same light-curve fitting procedure for all three of the STIS and WFC3 visits, but here describe the process for one visit.

3.4.1 White light-curve fit

For each visit (which comprises a set of time-series 1D spectra), we first created a white light curve by summing the counts of the 1D spectra across all wavelengths. The resulting time-series flux measurements show the transit signal modulated by systematic trends which correlate with *HST* phase, and the changing position of the spectrum on the detector. Such trends are commonly reported in STIS and WFC3 time-series data (e.g. Brown et al. 2001, Deming et al. 2013; Wakeford et al. 2016). Since we do not know the functional form of the systematic trends, Gibson et al. (2012) suggest treating the light curve as a Gaussian process (GP). Therefore, we follow the implementation of GPs for the *HST* light curves pioneered by Evans et al. (2013, 2018), except we use the PYTHON library for GP regression, George (Ambikasaran et al. 2015) rather than a custom code. Similarly to Evans et al. (2013, 2018), we used a squared-exponential kernel for the GP covariance matrix. We used three GP input variables – the *HST* orbital phase (ϕ), the position of the spectrum in the spatial direction on the detector (x), and the position in the dispersion direction (y). This gave four free GP parameters: the covariance amplitude (A), and a correlation length-scale for each of the four input variables: L_ϕ, L_x, and L_y for *HST* phase, x, and y respectively. We used BATMAN to model the transit light-curve signal, and fit for the planet-to-star radius ratio (R_p/R_*), fixing the remaining orbital parameters to the values given in Table 3. To model the stellar limb darkening, we fitted a four-parameter non-linear limb darkening law (Claret 2000) to the ATLAS stellar model (Castelli & Kurucz 2004) which most closely matches WASP-127 ($T_{\rm eff}$ = 5500 K, log g = 4.0 cgs). We also fit for the gradient (c_1) and y-intercept (c_0) of a linear trend in the out-of-transit baseline. Therefore, for the white light curve, we fit for seven free parameters overall: R_p/R_*, c_1, c_0, A, L_ϕ, L_x, and L_y. We used the MCMC package EMCEE (Foreman-Mackey et al. 2013) to marginalize over the parameter space of the model likelihood distribution. We used 80 walkers and ran chains for 500 steps, discarding the first 100 as burn-in before combining the walker chains into a single chain. The best-fitting results for the transit depths ($[R_p/R_*]^2$) are given in Table 3. Similarly, Figs 4, 5, and 6 show the best-fitting white light curves and their residuals for each visit. Figs B3, B4, and B5 show corner plots of the MCMC chains, which illustrate the posterior distributions for each

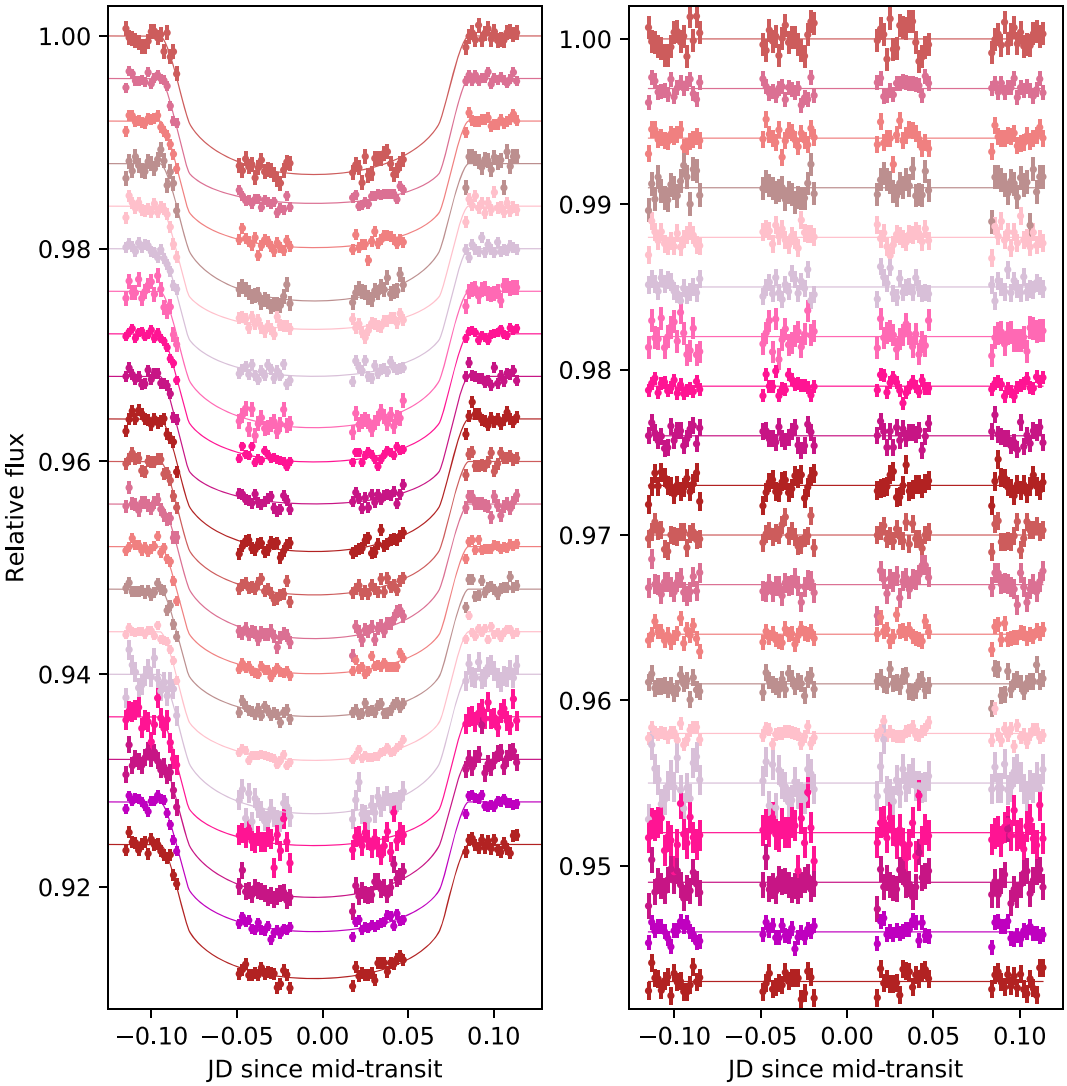

Figure 7. Spectroscopic light curves for WASP-127b using *HST*/STIS + G430L, covering the 2900–5700 Å wavelength range. (a) Points are light curves divided by systematics models, curves are best-fitting transit models. (b) Best-fitting model residuals. Arbitrary vertical offsets applied for clarity.

of the fits. The posterior distributions appear well sampled, and there are no problematic correlations between R_p/R_* and the other fitted parameters.

3.4.2 Spectroscopic light-curve fit

We used the same spectroscopic light-curve fitting procedure for each of the three *HST* visits. First, we binned each individual spectrum into spectroscopic channels (the wavelength ranges are given in Tables 4, 5, and 6), to make the spectroscopic light curves. We then employed a 'common-mode' correction to remove wavelength-independent systematic trends in the data (e.g. Evans et al. 2018). The process entails finding the systematic trends common to all wavelengths by dividing the white light curve by its best-fitting transit model, and then subtracting the result from each spectroscopic light curve before the fitting procedure. Similarly to the white light-curve fits, we fixed t_0 to the expected values found from our updated period and ephemeris, and fixed the orbital parameters to those derived from Lam et al. (2017), and wavelength-dependent limb darkening coefficients from the same ATLAS model which best describes WASP-127. Similarly to the white light-curve fit, we treat each spectroscopic light curve as a GP, using a squared-exponential kernel, and the same three GP input variables: (ϕ), (x), and (y). Therefore, for each spectroscopic channel the fitted parameters were R_p/R_*, c_1, c_0, A, L_ϕ, L_x, and L_y. We used the MCMC package EMCEE (Foreman-Mackey et al. 2013) to marginalize over the parameter space of the model likelihood distribution. We used 80 walkers and ran chains for 500 steps, discarding the first 100 as burn-in before combining the walker chains into a single chain. The best-fitting transit depths are given in Tables 4, 5, and 6 for the G430L, G750L, and G141 visits, respectively. The best-fitting spectroscopic light curves and their residuals are shown in Figs 7, 8, and 9. Example posterior distributions for individual spectroscopic light curves are shown in Figs B6, B7, and B8. The posterior distributions appear well sampled, and there are no problematic correlations between R_p/R_* and the other fitted parameters. We also ran the spectroscopic analysis for WFC3 G141 following the instrument systematic marginalization method outlined in Wakeford et al. (2016) and found the transmission

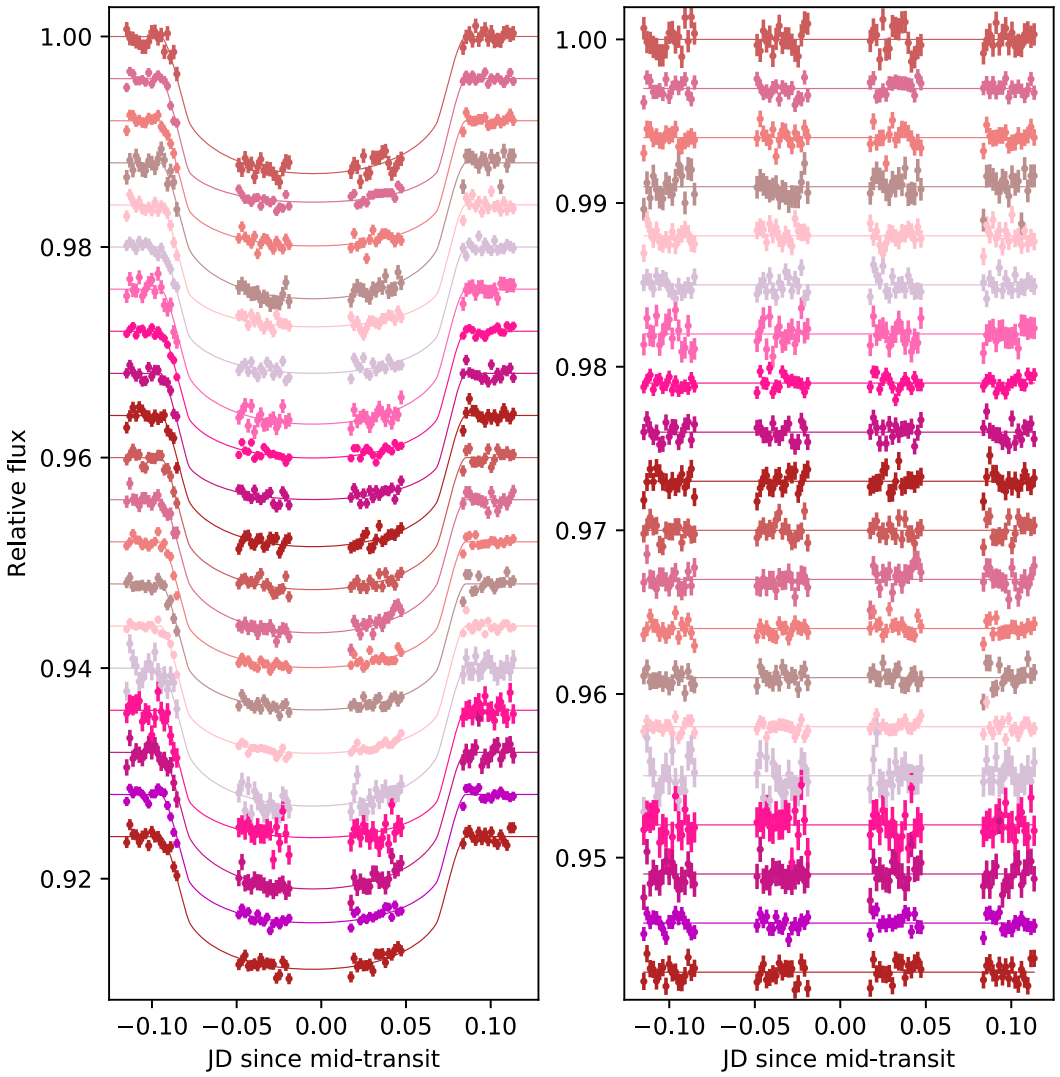

Figure 8. Spectroscopic light curves for WASP-127b using *HST*/STIS + G750L, covering the 5240–10 270 Å wavelength range. (a) Points are light curves divided by systematics models, curves are best-fitting transit models. (b) Best-fitting model residuals. Arbitrary vertical offsets applied for clarity.

spectral shape to be robust across the two systematic treatments with the absolute values of the measured depths within 1σ of each other. Similarly, we ran the spectroscopic analysis for both STIS visits following the marginalization method outlined in Nikolov et al. (2014), and found that the transit depths agreed within 1σ.

4 ATMO RETRIEVAL

For the combined STIS, WFC3, and *Spitzer* spectrum of WASP-127b, we performed an atmospheric retrieval analysis using a one-dimensional radiative transfer code for planetary atmospheres, ATMO (Amundsen et al. 2014; Tremblin et al. 2015, 2016, 2017; Goyal et al. 2018). Previous retrieval results using ATMO can be found in Wakeford et al. (2017a), Evans et al. (2017), and Mikal-Evans et al. (2019). ATMO can solve for the pressure–temperature (*P*–*T*) profile and chemical abundances that satisfy hydrostatic equilibrium and conservation of energy given a set of opacities (references for the opacity sources are listed in Goyal et al. 2018). It can also fit a parametrized *P*–*T* profile and chemical abundances to transmission spectroscopy data. For our retrievals, we used the paramatrized *P*–*T* profile of Guillot (2010) which gives three free parameters: the Planck mean thermal infrared opacity ($\kappa_{\rm IR}$); the ratio of optical to infrared opacities ($\gamma_{\rm O/IR}$); and an irradiation efficiency factor (β). The internal temperature was set to 500 K based on Thorngren, Gao & Fortney (2019). We used a relatively simple haze model:

$$\sigma(\lambda)_{\rm haze} = \delta_{\rm haze}\sigma_0(\lambda/\lambda_0)^{-\alpha_{\rm haze}}, \quad (2)$$

where $\sigma(\lambda)$ is the total scattering cross-section of the haze; $\delta_{\rm haze}$ is an empirical enhancement factor; σ_0 is the scattering cross-section of molecular hydrogen at 0.35 μm; and $\alpha_{\rm haze}$ sets the wavelength dependence of the scattering. For example, for pure Rayleigh scattering, $\alpha_{\rm haze} = 4$.

We performed two retrievals, one in chemical equilibrium with the elemental abundances free to vary and a free chemistry model where the molecular abundances were freely fit.

We coupled the forward ATMO model to a nested sampling algorithm (Feroz & Hobson 2008; Feroz, Hobson & Bridges 2009; Feroz et al. 2013) enabling Bayesian model comparison and marginalizing the posterior distribution.

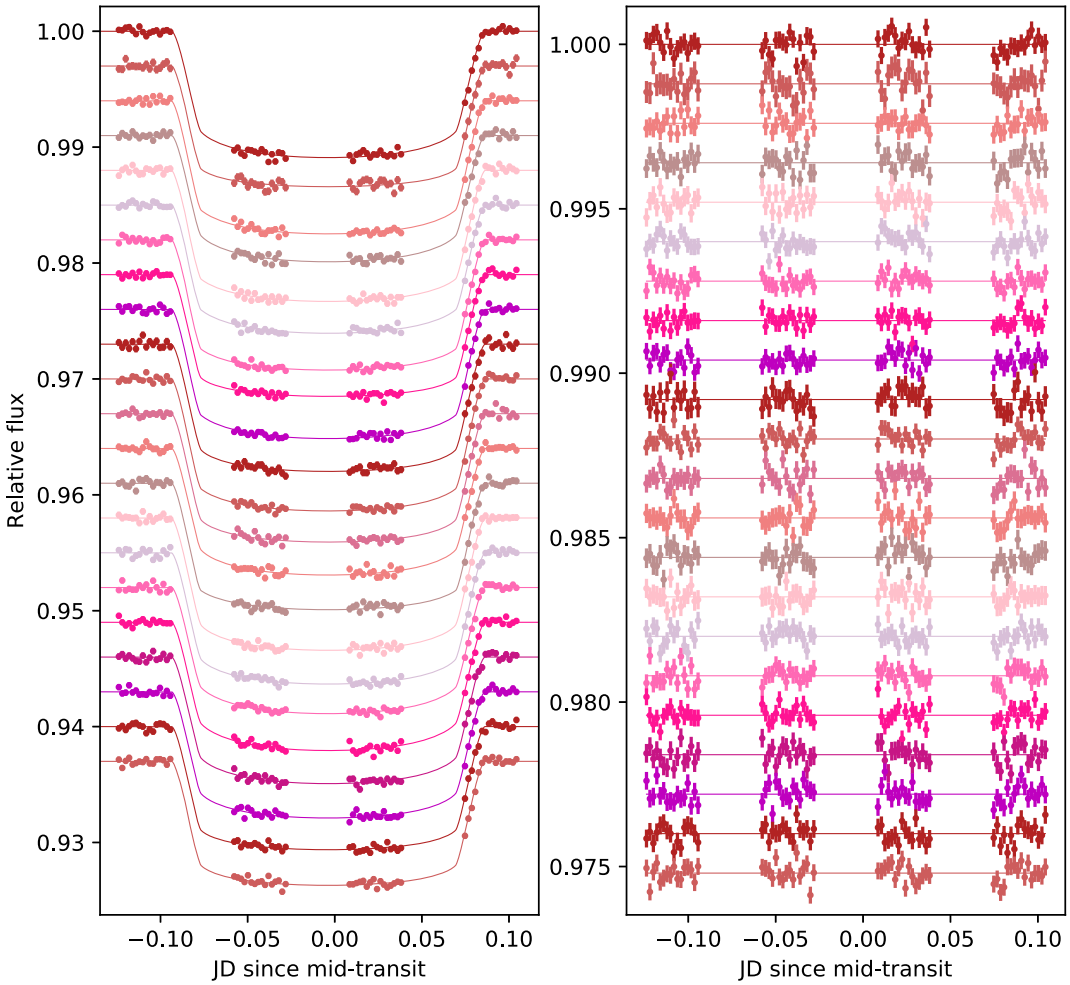

Figure 9. Spectroscopic light curves for WASP-127b using *HST*/WFC3 + G141, covering the 11 000–17 000 Å wavelength range. (a) Points are light curves divided by systematics models, curves are best-fitting transit models. (b) Best-fitting model residuals. Arbitrary vertical offsets applied for clarity.

For the model assuming chemical equilibrium, the elemental abundances for each model were freely fit and calculated in equilibrium on the fly. Five elements were selected to vary independently, as they are major species that are also likely to be sensitive to spectral features in the data, while the rest were varied by a trace metallicity parameter ($[Z_{trace}/Z_{\odot}]$). By varying the carbon, oxygen, and sodium elemental abundances ($[C/C_{\odot}]$, $[O/O_{\odot}]$, $[Na/Na_{\odot}]$) separately, we allow for non-solar compositions but with chemical equilibrium imposed such that each model fit has a chemically plausible mix of molecules given the retrieved temperatures, pressures, and underlying elemental abundances. Importantly, by varying both O and C separately (rather than a single C/O value) we alleviate an important modelling assumption that can affect the retrieved C/O value (see Drummond et al. 2019). For the spectral synthesis, we included the spectroscopically active molecules of H_2, He, H_2O, CO_2, CO, CH_4, NH_3, H_2S, HCN, C_2H_2, Na, K, Li, TiO, VO, Fe, FeH, SO_2, HCN, H_2S, PH_3, and H-. Rainout of condensate species was also included. The best-fit transmission spectra are shown in Fig. 10; the *P-T* profiles are shown in Fig. 11; the abundances of selected species as a function of pressure are shown in Fig. 12; and the posteriors are shown in Fig. 13. The final results are also given in Table 7, including the best-fitting model parameters and 1σ uncertainties (which correspond to the range of parameters which contain 68 per cent of the posterior samples). Good fits to the data were obtained, with the minimum χ^2 of 47.6 found for 55 degrees of freedom. We also calculated physically consistent *P–T* profiles in chemical and radiative equilibrium using the best-fitting elemental abundances and haze parameters from the chemical equilibrium retrieval (Fig. 11). For these numerically simulated *P–T* profiles, we varied the internal temperature of the planet, T_{int}, and its atmospheric heat recirculation factor, f_c. We reduce the incoming flux in the 1D column of the atmosphere by f_c to account for the effects of winds which redistribute stellar flux around the 3D planet, and the incidence angle of the flux.

In the free-chemistry model, we assumed that the volume mixing ratio (VMR) for each species was constant with pressure, and each molecule VMR was independently fit. We varied the H_2O, CO_2, CO, CH_4, Na, K, and FeH abundances. Li was not fit nor were TiO, VO, HCN, Fe, and C_2H_2 as no signs of them were observed in the data. The scattering haze scheme was the same as the equilibrium model. The results are shown in Figs 10, 11, and 14, and Table 8. The free-retrieval also resulted in a good fit, with a minimum χ^2 of 42.7 found for 52 degrees of freedom.

We ran two additional retrievals to test the influence of our choice of scattering haze scheme on our final results. First, we reran the chemical equilibrium model without any haze (i.e. a 'clear' atmosphere). The best-fitting model gave an extremely poor fit to

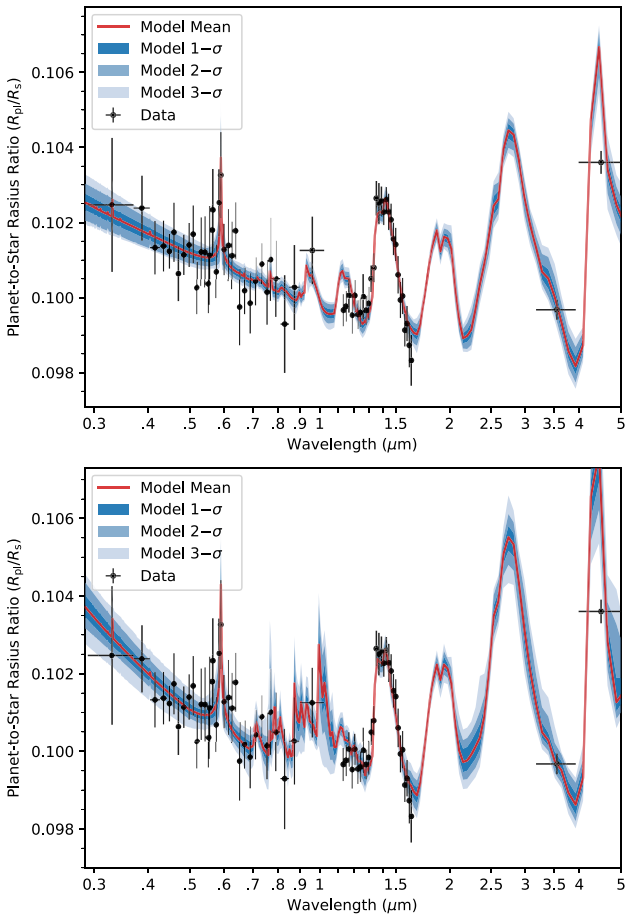

Figure 10. Transmission spectrum retrieval results from ATMO assuming chemical equilibrium (top) and free chemistry (bottom). The black points are the data, the red line is the median spectrum of the posterior distribution. The 1σ, 2σ, and 3σ model distributions are also shown (dark blue, blue, and light blue, respectively).

Table 7. Equilibrium chemistry retrieval results fitting to WASP-127b's transmission spectrum.

Parameter	Value	Prior range
$\chi^2_{\rm min}$	47.6	
$N_{\rm free}$	10	
$N_{\rm data}$	65	
$R_{\rm P,\ 1bar}$ [$R_{\rm J}$]	$1.3861^{+0.0050}_{-0.0058}$	1.24–1.52
$\log_{10}(\kappa_{\rm IR})$	$-2.99^{+0.85}_{-0.78}$	−5 to −0.5
$\log_{10}(\gamma_{\rm O/IR})$	$-1.92^{+1.29}_{-1.06}$	−4 to 1.5
β	$0.68^{+0.03}_{-0.05}$	0–2
$\ln(\delta_{\rm haze})^a$	$2.68^{+0.35}_{-0.29}$	−10 to 10
$\alpha_{\rm haze}{}^a$	$1.50^{+0.21}_{-0.27}$	0–5
$\log_{10}(Z_{\rm trace}/Z_\odot)^b$	$-0.17^{+0.42}_{-0.30}$	−1 to 2
$\log_{10}({\rm O/O}_\odot)$	$1.21^{+0.16}_{-0.17}$	−1 to 2
$\log_{10}({\rm C/C}_\odot)$	$1.41^{+0.17}_{-0.18}$	−1 to 2
$\log_{10}({\rm Na/Na}_\odot)$	$0.94^{+0.44}_{-0.58}$	−1 to 2

[a]The cloud and haze strengths are defined in Section 4.
[b]$\log_{10}({\rm Ztrace/Z}_\odot)$ is not the overall bulk metallicity but contains the abundances for trace species not otherwise individually fit (i.e. all except H, He, O, C, and Na).

Table 8. Free-chemistry retrieval results fitting to WASP-127b's transmission spectrum. VMR refers to the volume mixing ratio.

Parameter	Value	Prior range
$\chi^2_{\rm min}$	42.7	
$N_{\rm free}$	13	
$N_{\rm data}$	65	
$R_{\rm P,\ 1bar}$ [$R_{\rm J}$]	$1.4505^{+0.0075}_{-0.0061}$	1.24–1.52
$\log_{10}(\kappa_{\rm IR})$	$-3.41^{+0.79}_{-0.75}$	−5 to −0.5
$\log_{10}(\gamma_{\rm O/IR})$	$-1.07^{+0.92}_{-0.94}$	−4 to 1.5
β	$-0.092^{+0.078}_{-0.204}$	0–2
$\ln(\delta_{\rm haze})$	$-0.86^{+0.44}_{-0.63}$	−10 to 10
$\alpha_{\rm haze}$	$1.06^{+0.27}_{-0.22}$	0–5
VMR $\log_{10}(H_2O)$	$-4.16^{+0.17}_{-0.22}$	−14 to −1.3
VMR $\log_{10}(CO_2)$	$-5.52^{+0.46}_{-0.39}$	−14 to −1.3
VMR $\log_{10}(CO)$	$-7.87^{+2.68}_{-3.04}$	−14 to −1.3
VMR $\log_{10}(CH_4)$	$-10.18^{+1.72}_{-1.75}$	−14 to −1.3
VMR $\log_{10}(Na)$	$-6.99^{+0.35}_{-0.41}$	−14 to −1.3
VMR $\log_{10}(K)$	$-9.77^{+1.15}_{-1.26}$	−14 to −1.3
VMR $\log_{10}(FeH)$	$-7.56^{+0.36}_{-0.39}$	−14 to −1.3

the data, with a minimum χ^2 of 264 for 57 degrees of freedom. In particular, it could not produce enough opacity shortwards of 0.6 μm to match the data; and in order to match the muted water feature at 1.4 μm, it fit a much cooler *P–T* profile (500 K at pressures of 10^{-2}–10^{-6} bar, which seems implausible for a planet with an equilibrium temperature of 1400 K). We note that clear atmosphere solutions were allowed in all of our retrievals, since the uniform priors on the haze parameters encompass no-haze scenarios, but they were disfavoured. We therefore conclude that WASP-127b's atmosphere is unlikely to be entirely haze- or cloud-free.

Secondly, we ran the 'hazy' equilibrium chemistry retrieval with an additional, condensate 'cloud' absorption, which was assumed to have a grey wavelength dependence, and was calculated as

$$\kappa(\lambda)_{\rm cloud} = \delta_{\rm cloud}\kappa_{\rm H2}, \quad (3)$$

where $\kappa(\lambda)_{\rm c}$ is the 'cloud' absorption opacity, $\delta_{\rm cloud}$ is an empirical factor governing the strength of the grey scattering, and $\kappa_{\rm H2}$ is the scattering opacity due to H_2 at 0.35 μm. The previously described haze, $\sigma(\lambda)_{\rm haze}$, and the cloud, $\kappa(\lambda)_{\rm cloud}$, were added to the total gaseous scattering and absorption, respectively. Our best-fitting result from the haze-plus-cloud run provides an equally good fit to the data as the haze-only scheme, with a minimum χ^2 of 47.7 found for 53 degrees of freedom. The best-fitting spectrum is almost identical to the haze-only run (see Fig. 10), because the data favour a very low level of wavelength-independent absorption. The retrieved molecular abundances all fall within 1σ of the haze-only retrieved abundances. We therefore conclude that there is little evidence in the data for a grey absorbing cloud.

5 NEMESIS RETRIEVAL

We also performed an independent retrieval using the NEMESIS radiative transfer and retrieval tool. NEMESIS was originally developed for Solar system analysis (Irwin et al. 2008) and subsequently updated for the study of exoplanets (e.g. Lee, Fletcher & Irwin 2012; Barstow et al. 2017). More recent upgrades have included incorporating the PYMULTINEST nested sampling algorithm (Feroz & Hobson 2008; Feroz et al. 2009, 2013; Buchner et al. 2014; Krissansen-Totton et al.

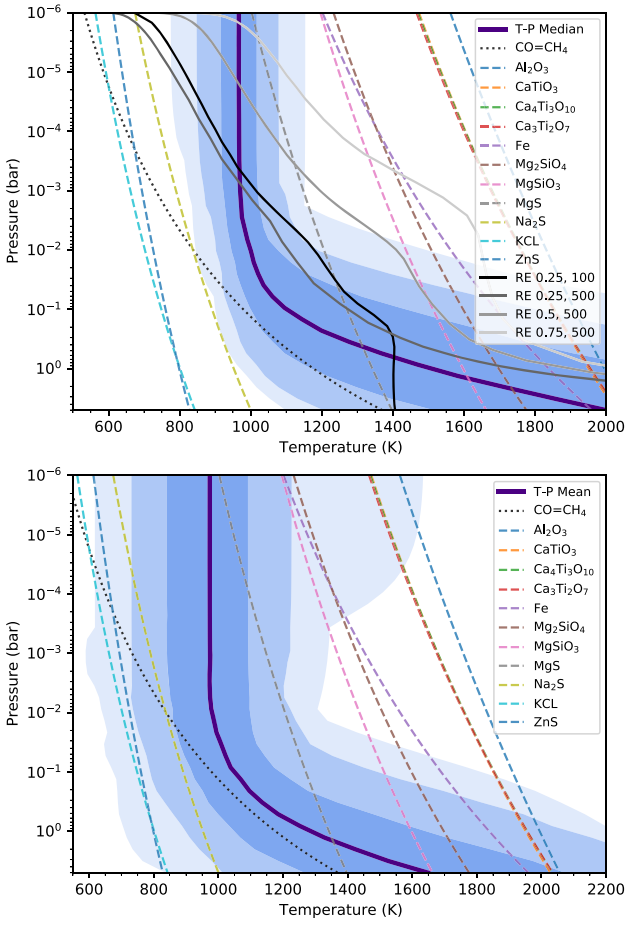

Figure 11. *P–T* profile retrieval results from ATMO assuming chemical equilibrium (top) and free chemistry (bottom). The solid purple line is the median profile of the posterior distribution; the dark blue, blue, and light blue shaded regions are the 1σ, 2σ, and 3σ model distributions. The dashed lines are cloud condensation curves calculated at a metallicity of $10\times$ solar from Visscher, Lodders & Fegley (2006, 2010) and Wakeford et al. (2017b). The three grey solid lines in the top panel are converged *P–T* profiles in chemical and radiative equilibrium ('RE'), each with an internal temperature ($T_{\rm int}$) of 500 K, and a heat recirculation factor ($f_{\rm c}$) of 0.25, 0.5, and 0.75, respectively. They use the haze and elemental abundances from the chemical equilibrium retrieval. Black solid line is a cloud-free converged *T–P* profile at $10\times$ solar abundance for WASP-127b from Goyal et al. (2020), with $T_{\rm int} = 100$K and $f_{\rm c} = 0.25$.

Table 9. References for opacity sources used in NEMESIS retrieval.

Opacity source	Reference
CO	Li et al. (2015)
CO_2	Tashkun & Perevalov (2011)
CH_4	Yurchenko et al. (2017)
H_2O	Polyansky et al. (2018)
H_2–H_2	Borysow (2002); Borysow & Frommhold (1990)
H_2–He	Borysow & Frommhold (1989); Borysow, Frommhold & Moraldi (1989)
Na	Kramida et al. (2019)
K	Kramida et al. (2019)

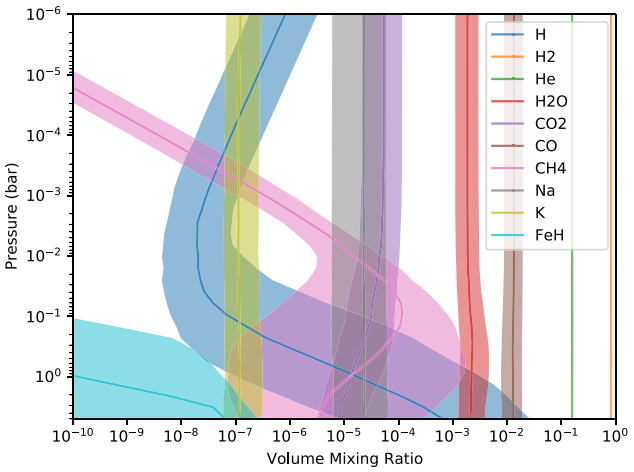

Figure 12. Retrieved chemical abundances as a function of pressure from the ATMO chemical equilibrium retrieval, for selected species.

2018). NEMESIS uses the correlated-k approximation for tabulating atomic and molecular opacities (Lacis & Oinas 1991), which results in a rapid forward model computation. NEMESIS incorporates absorption from Na, K, H_2O, CO_2, CO, and CH_4, as well as collision-induced absorption due to H_2 and He. Sources of absorption line data are included in Table 9. K tables used in this work are as compiled in Chubb et al. (2020). The retrieved temperature profile follows the specification of Guillot (2010), and the haze scheme is the same as that described in Section 4, except we allow for incomplete ('patchy') coverage, as described in MacDonald & Madhusudhan (2017). The best-fitting transmission spectrum is shown in Fig. 15, the *P-T* profile in Fig. 16, and the posterior distributions in Fig. 17.

6 RESULTS AND DISCUSSION

The transmission spectrum of WASP-127b shows absorption by sodium, water, and either CO_2 or CO (see Fig. 18). Longward of ~0.5 μm, the optical spectrum is in good agreement with the results of Chen et al. (2018), albeit with a few points which differ with a statistically significant margin. To quantify the detection significances of sodium and water, we calculated the Bayesian Information Criterion (BIC) for our best-fitting ATMO free-chemistry model ($\rm BIC_{\it i,model}$); and a straight line fit through the data range of interest ($\rm BIC_{\it i,line}$). For sodium, we used all *HST*/STIS data at wavelengths shorter than 0.722 μm, because at these wavelengths our models suggest the only opacity sources are sodium and a scattering haze. For these 28 data points, we found $\rm BIC_{Na,model} = 22.9$ and $\rm BIC_{Na,line} = 27.9$, with three and two free parameters, respectively. The ATMO model provides a better fit to the data at 1.7σ, which is a detection of low significance, compared to the previous detection of sodium at 4.1σ for WASP-127b by Chen et al. (2018). For water, we used all of the data from HST/WFC3, and found $\rm BIC_{H_2O,model} = 35.9$ and $\rm BIC_{H_2O,line} = 228.9$, which gives a detection significance of 13.7σ. For context, one of the strongest water absorption features measured in an exoplanet atmosphere, also using a single *HST*/WFC3 transit observation in spatial scan mode, was made by Kreidberg et al. (2018) for WASP-107b – a similarly low-density gas-giant exoplanet, but cooler than WASP-127b. They detected water in WASP-107b's atmosphere at a confidence of 6.5σ. To the best of our knowledge, the data set

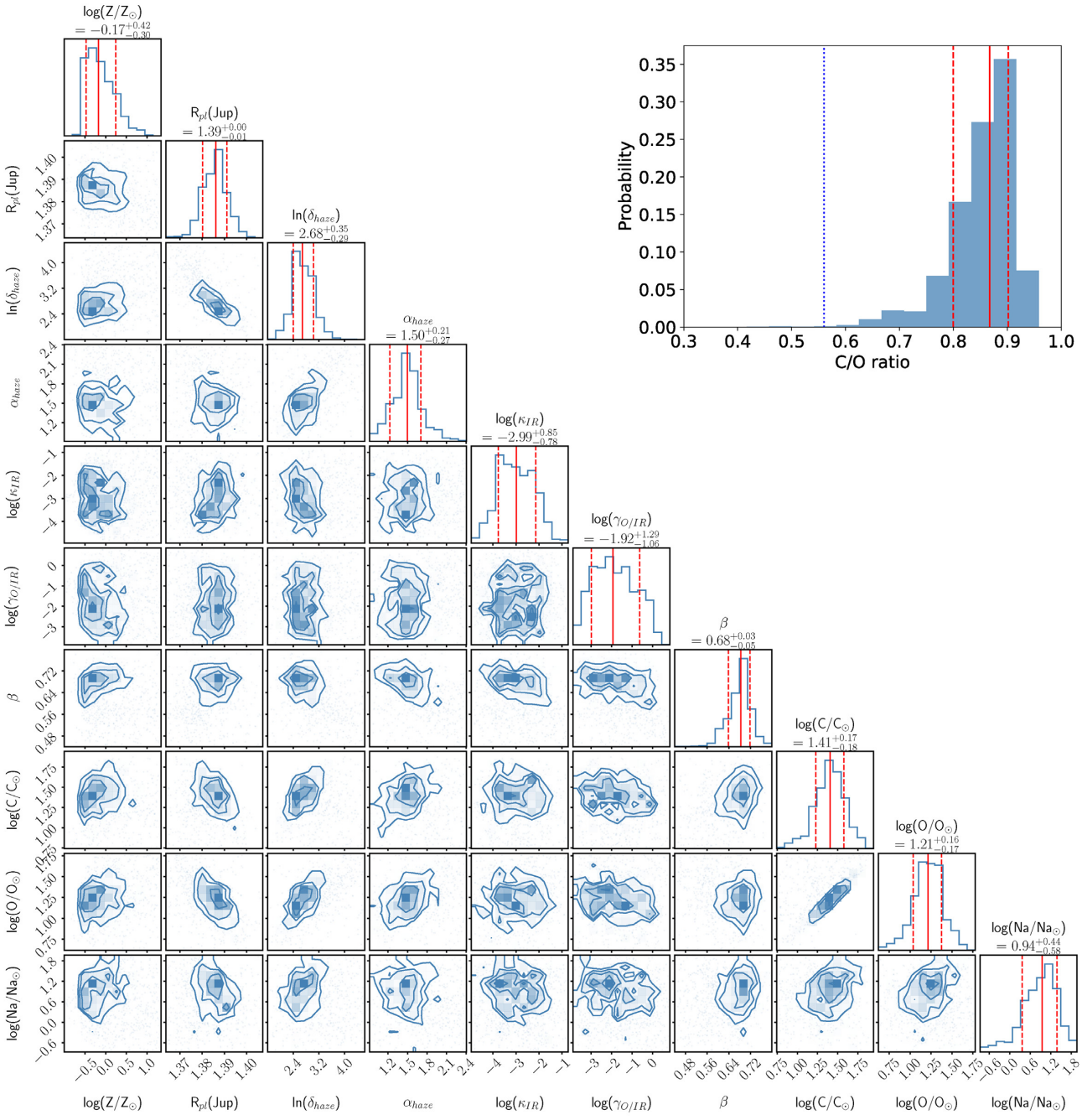

Figure 13. Posterior distributions for atmospheric retrieval fit from ATMO for WASP-127b assuming chemical equilibrium. Solid red lines show median values; dashed red lines contain 68 per cent of samples. The posterior distribution of the C/O ratio is also shown, with the solar value shown as the blue dotted line.

presented here shows the strongest water absorption feature (in terms of detection significance) of any exoplanet observed with *HST*/WFC3.

The sodium and water abundances are well-constrained by our ATMO retrievals, and are supersolar. Our free-chemistry fit gives a water abundance of $-4.16^{+0.17}_{-0.22}$, which is consistent with, but better-constrained than the value of $\log(H_2O) = -2.50^{+0.94}_{-4.56}$ found by Chen et al. (2018), who observed unresolved water absorption. We retrieved a lower sodium abundance of $-6.99^{+0.35}_{-0.41}$, compared to the very supersolar value of $\log(Na) = -3.17^{+1.03}_{-1.46}$ from Chen et al. (2018) ($\log_{10}[Na_\odot] = -5.76$; Asplund et al. 2009). The NEMESIS retrieval gives water and sodium abundances of $-3.40^{+0.21}_{-0.22}$ and $-6.47^{+0.52}_{-0.78}$ respectively, which both agree with the ATMO abundances at the 1σ–2σ level. Therefore, despite the difference in the cloud scheme and retrieved *P*–*T* profiles (see Fig. 11 versus Fig. 17), our main abundance constraints are consistent across the two retrieval codes.

Both our free and equilibrium ATMO retrievals favour supersolar abundances and strong absorption by CO_2. The 4.5 μm absorption feature in the transmission spectrum is unusually strong, and to the best of our knowledge, no broad-band transmission spectrum to date has shown such a strong feature in this wavelength band (e.g. Sing

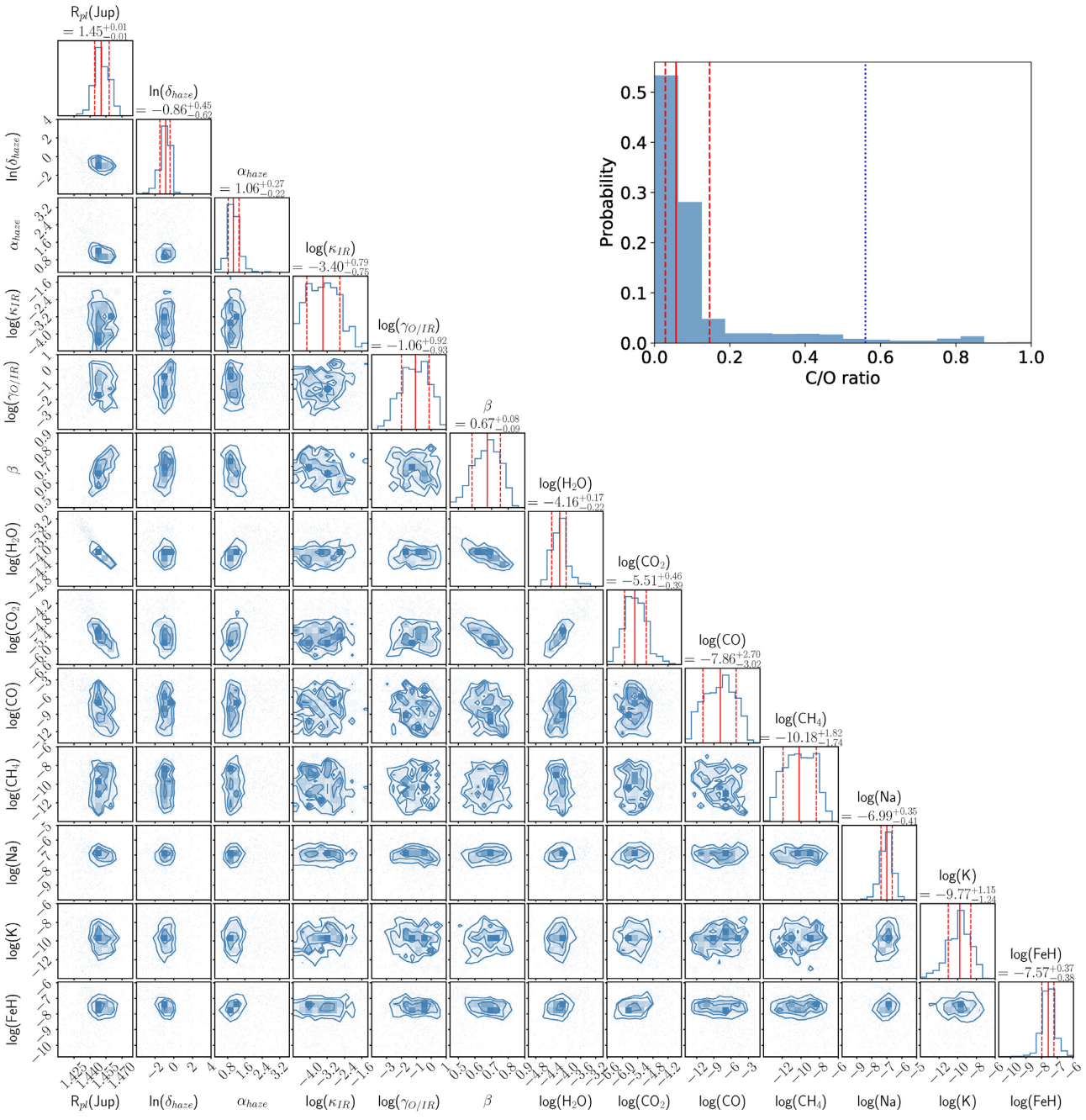

Figure 14. Similar as Fig. 13 but for freely fit chemistry.

et al. 2016). Both retrievals fit the feature with CO_2, which is an indication of high metallicities, as there is a well-studied sensitivity of CO_2 to metallicity (e.g. Lodders & Fegley 2002; Fortney 2005; Burrows; Budaj & Hubeny 2008; Fortney et al. 2008; Line; Liang & Yung 2010; Moses et al. 2011; Heng & Lyons 2016; Goyal et al. 2018). The free-chemistry model gives a VMR abundance of $-3.83^{+0.27}_{-0.23}$ which is somewhat lower compared to the VMR at 1 mbar from the best-fitting equilibrium chemistry model of -2.7 ± 0.2. These values correspond to supersolar metallicities, with the chemical equilibrium retrievals finding O and C are 16 and 26× solar respectively, with both values well-constrained with 1σ uncertainties of ∼0.2 dex (see Table 7). With Na, H_2O, and CO_2 all showing signatures of supersolar metallicities, WASP-127b is currently one of the few such cases where the abundances of multiple species can be constrained within the planet's atmosphere.

Our *HST*/STIS spectrum also shows wavelength-dependent scattering in the optical. We do not see the sharp rise blueward of 5600 Å that Chen et al. (2018) report from the ground-based NOT data. Instead, we find a shallower slope, presumably caused by scattering off some kind of condensate/haze material made from small (<1 μm) particles, which slopes down into the near-infrared. We note that ground-based optical transmission spectra frequently suffer from differential atmospheric extinction problems at <0.4 μm. The *HST* spectrum also contains little evidence of K, and no evidence of Li,

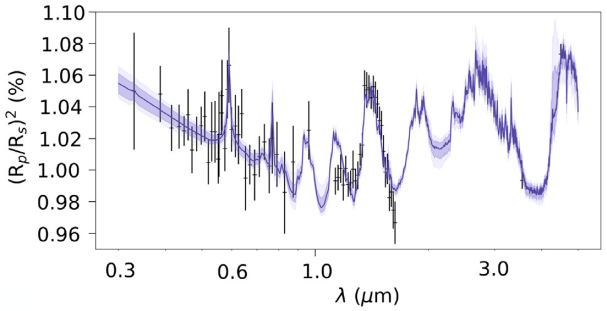

Figure 15. Transmission spectrum retrieval results from NEMESIS.

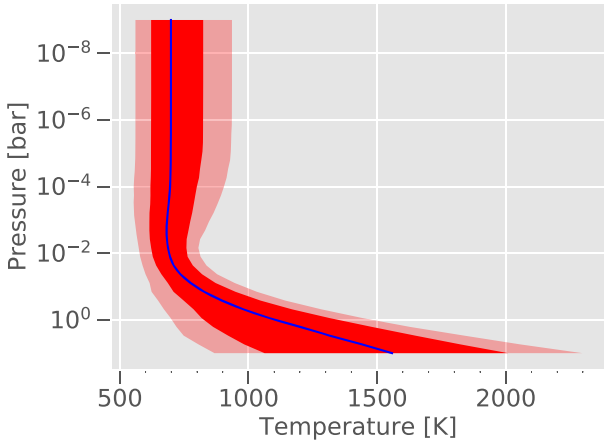

Figure 16. *P–T* profile retrieval results from NEMESIS.

which were previously reported to be present from ground-based spectroscopy.

To highlight the evidence for CO_2 in the transmission spectrum, in Fig. 18 we show three ATMO model atmospheres: our best-fitting model from the free-chemistry retrieval; a model with all of the same parameters as the best fit, except the CO_2 abundance, which is set to zero; and a third model with both CO and CO_2 abundances set to zero. The strong absorption feature centred on the 4.5 μm *Spitzer* channel disappears in the latter two models. With only *Spitzer* photometry, however, the contribution of CO to the 4.5 μm point complicates the interpretation of the C/O ratio. Theoretical models have found that CO should be the dominant carbon-bearing molecule for hydrogen-dominated atmospheres above 1000 K (e.g. Lodders & Fegley 2002; Heng & Lyons 2016), and CO has been detected at high resolution in hot Jupiter atmospheres (e.g. Snellen et al. 2010). In our equilibrium chemistry retrieval, CO is at least 100× more abundant than CO_2 (see Fig. 12). However, at 4.5 μm the CO_2 opacity is much stronger and dominates over the CO contribution even though CO has much higher VMR concentrations. In the free-chemistry retrieval, the CO VMR is not constrained by the data – only an upper limit to the CO is found, as very high values affect the mean molecular weight, and the data are consistent with no CO contribution. The lack of a CO feature in the WFC3 data further pushes the free-chemistry retrieval to prefer CO_2 over CO. With CO constrained through chemistry in one retrieval and unconstrained in the free case, the C/O ratios obtained are vastly different. In the chemical-equilibrium case, a supersolar C/O is found (see Fig. 13) while in the free case a subsolar C/O ratio is found (Fig. 14). This finding highlights the extreme sensitivity and degeneracies of measuring the C/O ratio with a free-chemistry retrieval model, as all major molecular species have to be well constrained by the data. For a hot Jupiter such as WASP-127b, we consider a scenario with all of the carbon found in CO_2 and little to none in CO to be thermochemically implausible, as no obvious non-equilibrium mechanism would deplete CO by many orders of magnitude while enhancing CO_2. This situation is unlike CH_4, where dynamical mixing and vertical quenching can dramatically enhance CH_4 (e.g. Cooper & Showman 2006; Moses et al. 2011; Tsai et al. 2017; Drummond et al. 2018a, b). With only one photometric data point at 4.5 μm, it is currently impossible to fully disentangle the contribution of both CO and CO_2 in a model-independent way. Further transmission spectroscopy observations of WASP-127b at high resolution with the *JWST* will clarify which is the dominant carbon-bearing molecule in WASP-127b's atmosphere, and allow stronger constraints to be placed on its carbon-to-oxygen ratio.

Although we do not resolve any absorption features of iron hydride (FeH), our best-fitting, free-chemistry retrieval from ATMO fits the data better at a confidence of 2.5σ compared to free-chemistry retrievals run without FeH. The retrieved VMR was $-7.56^{+0.36}_{-0.39}$, which is significantly higher than expected from solar abundances. Fig. 12 shows that in chemical equilibrium, such high abundances of FeH can be expected deeper in the atmosphere, at pressures of around 60 bars. There have been several previous reports of FeH in exoplanet atmospheres, including WASP-127b (e.g. Sotzen et al. 2020 and Skaf et al. 2020). However, there may be other, unresolved absorbers in the 0.8–1.2 μm wavelength range, and it is unclear how such high abundances of FeH could be present at such low pressures in WASP-127b's atmosphere. Since the ATMO chemical equilibrium model (which folds the FeH abundance into $\log_{10}(Z_{trace}/Z_{\odot})$) and the free-chemistry model are similarly favoured by the data, with a reduced χ^2 of 0.86 and 0.81, respectively, we do not have enough evidence to definitively detect FeH.

Our retrieved temperature profiles from ATMO (Fig. 11) agree fairly well with the converged *P–T* profile for WASP-127b from Goyal et al. (2020). Of the converged *P–T* profiles that we ran with an internal temperature of 500 K, and varying heat redistribution factors, the model with $f_c = 0.25$ is most similar to that from our chemical equilibrium retrieval. This suggests that at WASP-127b's terminator, where our transmission signal originates, only 25 per cent of the incoming stellar irradiation on the planet's dayside is required to match our observed *P–T* profile and abundances in chemical equilibrium. This is as expected from a hot, tidally locked planet which likely reradiates some of the flux received on its dayside before it can be advected around the planet by winds. Our retrieved NEMESIS *P–T* profile is noticeably cooler than those from ATMO (Fig. 16), which may be a result of the greater degree of flexibility in the *P–T* profile fit, and the patchy haze scheme that may allow colder temperatures to mute absorption features, instead of hazes.

To place the abundance measurements in a wider context, we plot the measured atmospheric metallicity from the equilibrium chemistry retrieval against other exoplanet measurements and the Solar system giant planets. Fig. 19 shows the measured metallicity of the Solar system giant planets via their abundance of CH_4 (Wong et al. 2004; Fletcher et al. 2011; Karkoschka & Tomasko 2011; Sromovsky, Fry & Kim 2011), and exoplanets via predominantly their H_2O abundance (Kreidberg et al. 2014, 2015; Brogi et al. 2017; Morley et al. 2017; Wakeford et al. 2017a, 2018; Benneke et al. 2019; Chachan et al. 2019; Bruno et al. 2020). The trend of increased atmospheric metallicity with decreasing mass seen for

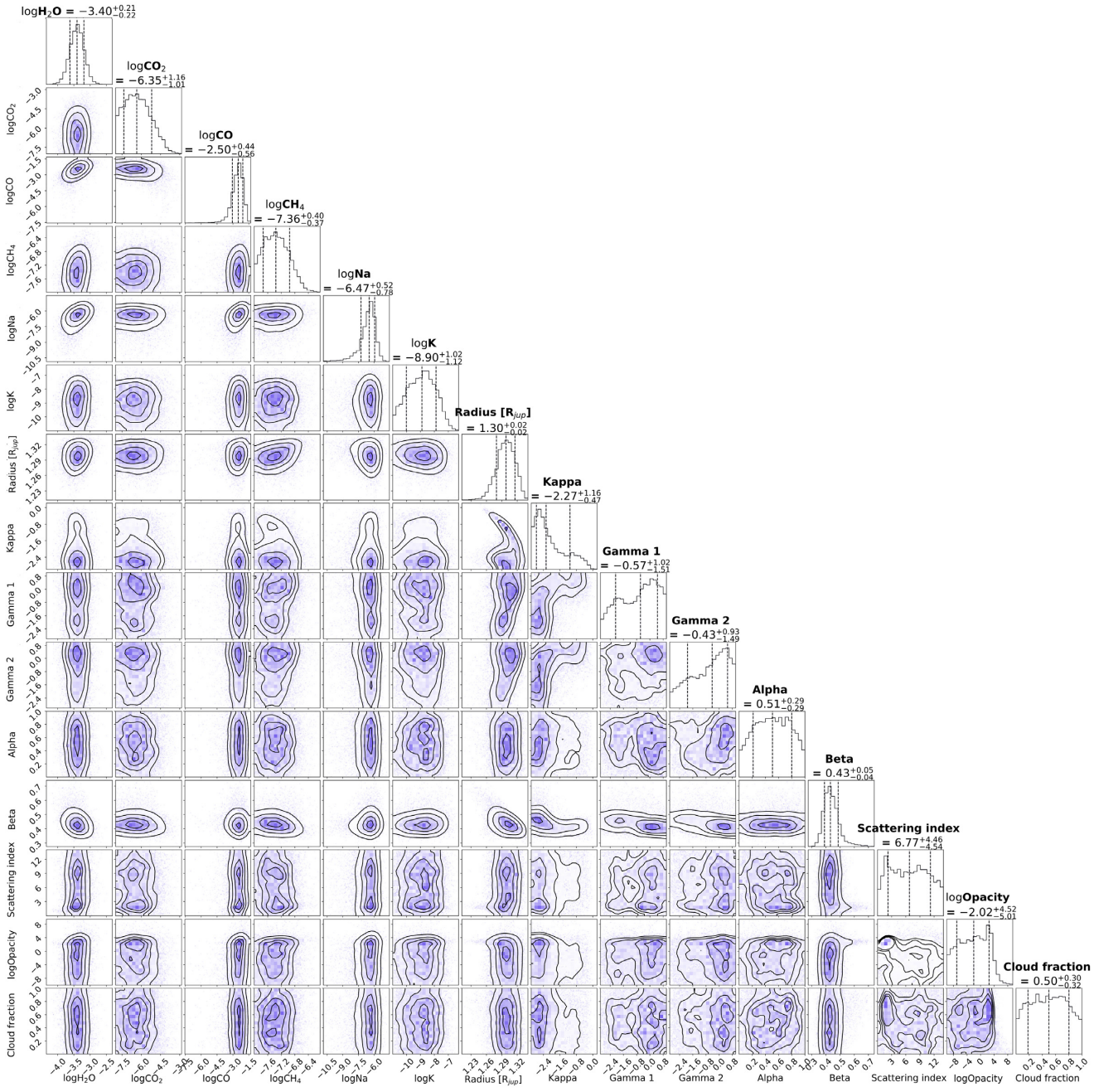

Figure 17. Posterior distributions for atmospheric retrieval fit from NEMESIS for WASP-127b.

the Solar system giant planets is thought to be indicative of core accretion formation. The measurements of WASP-127b place it in the middle of the exoplanet distribution and along the trend shown by the Solar system giants. However, for the current exoplanet population, all of which are orbiting much closer to their stars than their Solar system mass counterparts, there is no significant trend in the data.

Overall, we have observed evidence of strong absorption features from several atomic and molecular species, which means that the level of clouds and potential hazes in WASP-127b is not so strong as to prevent the determination of its atmospheric composition. We find the atmosphere has a supersolar metallicity which is traced by several species (H_2O, Na, and CO_2). Assuming chemical equilibrium, these three species have an average metallicity of $17 \pm 4\times$ solar. While there has been considerable spread in retrieved metallicities of exoplanets to date, WASP-127b is in good agreement with the mass–metallicity trend of the Solar system (see Fig. 19). This evidence, combined with a long transit duration, means that WASP-127b is the ideal benchmark exoplanet for measuring chemical abundances of exoplanet atmospheres and should be one of the prime targets for *JWST*. In particular, the hint of a large absorption feature around 4.5 μm is strong evidence that future observations of WASP-127b with *JWST* will be able to measure the abundances of carbon-bearing species in its atmosphere.

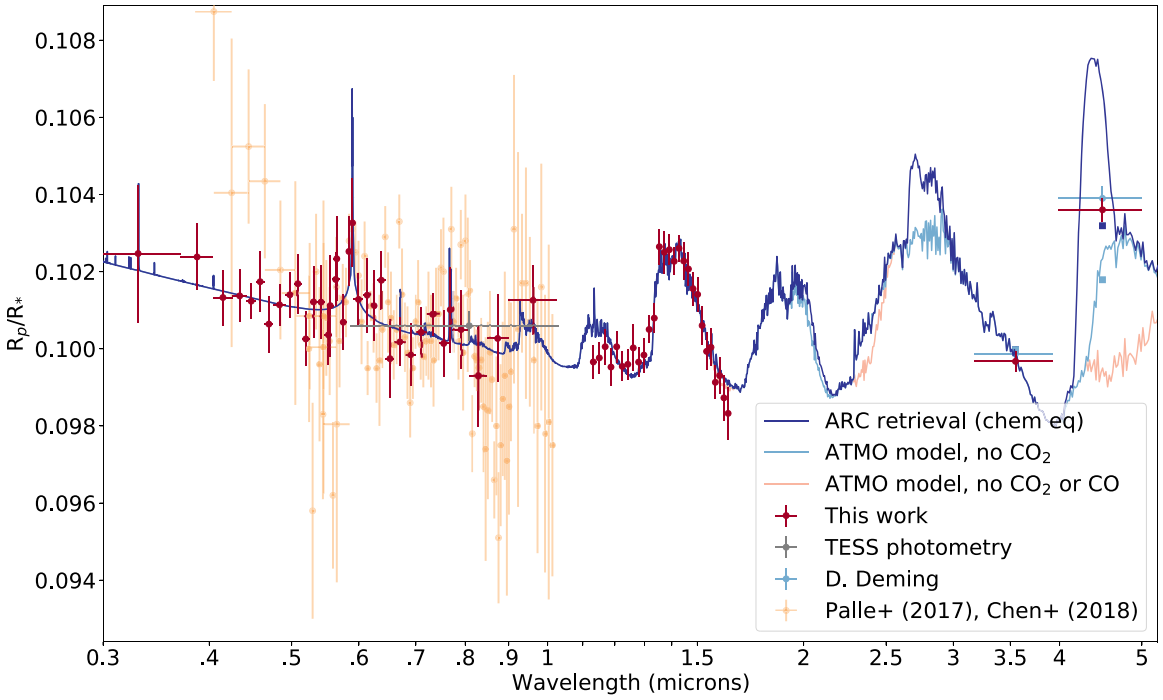

Figure 18. Transmission spectrum for WASP-127b. Red data points are from this work, blue data points are from an independent analysis of the *Spitzer* light curves from D. Deming. Yellow points are previously published data from Palle et al. (2017) and Chen et al. (2018) using ground-based telescopes. Dark blue line is our best-fitting retrieval models using ARC and MPFIT, light blue line is same model with CO_2 abundance set to zero. Square points show models binned to the resolution of the *Spitzer* data.

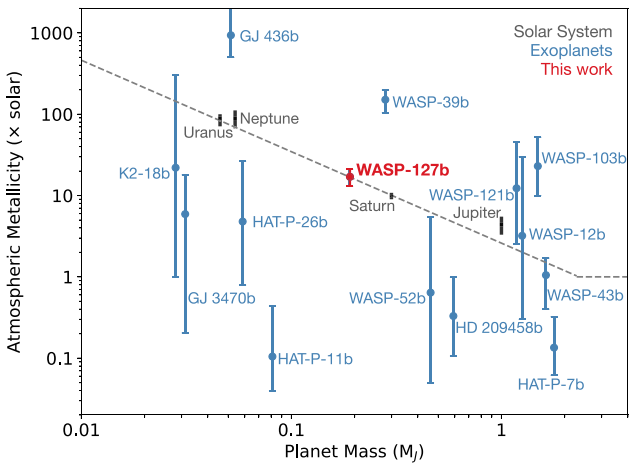

Figure 19. Mass against atmospheric metallicity for the Solar system giant planets (grey squares) and measured exoplanets (blue and red dots). The trend seen in the Solar system giants is taken to indicate formation via core accretion. Our measurement of WASP-127b's atmospheric metallicity using the equilibrium chemistry oxygen abundance as proxy (red dot) fits squarely on this trend line. However, including the other measured exoplanets there is no clear trend seen throughout the measured exoplanet population.

ACKNOWLEDGEMENTS

This work is based on observations made with the NASA/European Space Acency *Hubble Space Telescope* that were obtained at the Space Telescope Science Institute (STScI), which is operated by the Association of Universities for Research in Astronomy, Inc. Support for this work was provided by NASA through grants under the HST-GO-14619 program from the STScI. A portion of this work is based on observations made with the Spitzer Space Telescope, which is operated by the Jet Propulsion Laboratory, California Institute of Technology under a contract with NASA. ALC is funded by a UK Science and Technology Facilities (STFC) studentship. This work made use of the PYTHON package CORNER (Foreman-Mackey 2016). JJS thanks the anonymous reviewer for productive comments.

DATA AVAILABILITY

Raw *HST* data frames are publicly available online at the Mikulski Archive for Space Telescopes (MAST; https://archive.stsci.edu). Raw Spitzer data frames are publicly available at the NASA/IPAC Infrared Science Archive (IRSA; https://sha.ipac.caltech.edu/applications/Spitzer/SHA/)

REFERENCES

Ambikasaran S., Foreman-Mackey D., Greengard L., Hogg D. W., O'Neil M., 2015, IEEE Trans. Pattern Anal. Mach. Intell., 38, 252
Amundsen D. S., Baraffe I., Tremblin P., Manners J., Hayek W., Mayne N. J., Acreman D. M., 2014, A&A, 564, A59
Asplund M., Grevesse N., Sauval A. J., Scott P., 2009, ARA&A, 47, 481
Barstow J. K., Aigrain S., Irwin P. G. J., Sing D. K., 2017, ApJ, 834, 50
Benneke B. et al., 2019, Nat. Astron., 3, 813
Borysow A., 2002, A&A, 390, 779
Borysow A., Frommhold L., 1989, ApJ, 341, 549
Borysow A., Frommhold L., 1990, ApJ, 348, L41
Borysow A., Frommhold L., Moraldi M., 1989, ApJ, 336, 495
Brogi M., Line M., Bean J., Désert J.-M., Schwarz H., 2017, ApJ, 839, L2
Brown T. M., Charbonneau D., Gilliland R. L., Noyes R. W., Burrows A., 2001, ApJ, 552, 699

Bruno G. et al., 2020, MNRAS, 491, 5361
Buchner J. et al., 2014, A&A, 564, A125
Burrows A., Budaj J., Hubeny I., 2008, ApJ, 678, 1436
Castelli F., Kurucz R. L., 2003, in Piskunov N., Weiss W. W., Gray D. F., eds, Proc. IAU Symp. 210, Modelling of Stellar Atmospheres, Poster Contributions. Astron. Soc. Pac., San Francisco, p. A20
Chachan Y. et al., 2019, AJ, 158, 244
Charbonneau D., Brown T. M., Noyes R. W., Gilliland R. L., 2002, ApJ, 568, 377
Chen G. et al., 2018, A&A, 616, A145
Chubb K. L., 2020, preprint (arXiv:2009.00687)
Claret A., 2000, A&A, 363, 1081
Cooper C. S., Showman A. P., 2006, ApJ, 649, 1048
Deming D., Seager S., Richardson L. J., Harrington J., 2005, Nature, 434, 740
Deming D. et al., 2013, ApJ, 774, 95
Deming D. et al., 2015, ApJ, 805, 132
Drummond B. et al., 2018a, ApJ, 855, L31
Drummond B., Mayne N. J., Manners J., Baraffe I., Goyal J., Tremblin P., Sing D. K., Kohary K., 2018b, ApJ, 869, 28
Drummond B., Carter A. L., Hébrard E., Mayne N. J., Sing D. K., Evans T. M., Goyal J., 2019, MNRAS, 486, 1123
Evans T. M. et al., 2013, ApJ, 772, L16
Evans T. M., Aigrain S., Gibson N., Barstow J. K., Amundsen D. S., Tremblin P., Mourier P., 2015, MNRAS, 451, 680
Evans T. M. et al., 2017, Nature, 548, 58
Evans T. M. et al., 2018, AJ, 156, 283
Feroz F., Hobson M. P., 2008, MNRAS, 384, 449
Feroz F., Hobson M. P., Bridges M., 2009, MNRAS, 398, 1601
Feroz F., Hobson M. P., Cameron E., Pettitt A. N., 2019, OJAp, 2, 10
Fletcher L. N., Baines K. H., Momary T. W., Showman A. P., Irwin P. G. J., Orton G. S., Roos-Serote M., Merlet C., 2011, Icarus, 214, 510
Foreman-Mackey D., 2016, J. Open Source Softw., 1, 24
Foreman-Mackey D., Hogg D. W., Lang D., Goodman J., 2013, PASP, 125, 306
Fortney J. J., 2005, MNRAS, 364, 649
Fortney J. J., Lodders K., Marley M. S., Freedman R. S., 2008, ApJ, 678, 1419
Gibson N. P., Aigrain S., Roberts S., Evans T. M., Osborne M., Pont F., 2012, MNRAS, 419, 2683
Goudfrooij P., Christensen J. A., 1998, STIS Instrument Science Report, 1998, 29
Goyal J. M. et al., 2018, MNRAS, 474, 5158
Goyal J. M. et al., 2020, MNRAS, 498, 4680
Guillot T., 2010, A&A, 520, A27
Heng K., Lyons J. R., 2016, ApJ, 817, 149
Huitson C. M., Sing D. K., Vidal-Madjar A., Ballester G. E., Lecavelier des Etangs A., Désert J.-M., Pont F., 2012, MNRAS, 422, 2477
Huitson C. M. et al., 2013, MNRAS, 434, 3252
Irwin P. G. J. et al., 2008, J. Quant. Spectrosc. Radiat. Transfer, 109, 1136
Jenkins J. M. et al., 2016, in Chiozzi G., Guzman J. C., eds, Proc. SPIE Conf. Ser. Vol. 9913, Software and Cyberinfrastructure for Astronomy IV. SPIE, Bellingham, p. 99133E
Karkoschka E., Tomasko M. G., 2011, Icarus, 211, 780
Katsanis R. M., McGrath M. A., 1998, STIS Instrument Science Report, 98, 14
Kramida A., Ralchenko Y., Reader J., NIST ASD Team, 2019, NIST Atomic Spectra Database, National Institute of Standards and Technology, Gaithersburg, MD
Kreidberg L., 2015, PASP, 127, 1161
Kreidberg L. et al., 2014, ApJ, 793, L27
Kreidberg L. et al., 2015, ApJ, 814, 66
Kreidberg L., Line M. R., Thorngren D., Morley C. V., Stevenson K. B., 2018, ApJ, 858, L6
Krissansen-Totton J., Garland R., Irwin P., Catling D. C., 2018, AJ, 156, 114
Lacis A. A., Oinas V., 1991, J. Geophys. Res., 96, 9027
Lam K. W. F. et al., 2017, A&A, 599, A3
Lee J. M., Fletcher L. N., Irwin P. G. J., 2012, MNRAS, 420, 170
Li G., Gordon I. E., Rothman L. S., Tan Y., Hu S.-M., Kassi S., Campargue A., Medvedev E. S., 2015, ApJS, 216, 15
Line M. R., Liang M. C., Yung Y. L., 2010, ApJ, 717, 496
Lodders K., Fegley B., 2002, Icarus, 155, 393
MacDonald R. J., Madhusudhan N., 2017, MNRAS, 469, 1979
Mandel K., Agol E., 2002, ApJ, 580, L171
Mikal-Evans T. et al., 2019, MNRAS, 488, 2222
Morley C. V., Knutson H., Line M., Fortney J. J., Thorngren D., Marley M. S., Teal D., Lupu R., 2017, AJ, 153, 86
Moses J. I. et al., 2011, ApJ, 737, 15
Nikolov N., Chen G., Fortney J. J., Mancini L., Southworth J., van Boekel R., Henning T., 2013, A&A, 553, A26
Nikolov N. et al., 2014, MNRAS, 437, 46
Nikolov N. et al., 2015, MNRAS, 447, 463
Palle E. et al., 2017, A&A, 602, L15
Polyansky O. L., Kyuberis A. A., Zobov N. F., Tennyson J., Yurchenko S. N., Lodi L., 2018, MNRAS, 480, 2597
Pont F., Sing D. K., Gibson N. P., Aigrain S., Henry G., Husnoo N., 2013, MNRAS, 432, 2917
Ricker G. R. et al., 2015, J. Astron. Telesc. Instrum. Syst., 1, 014003
Sing D. K., 2010, A&A, 510, A21
Sing D. K. et al., 2011, MNRAS, 416, 1443
Sing D. K. et al., 2013, MNRAS, 436, 2956
Sing D. K. et al., 2016, Nature, 529, 59
Skaf N. et al., 2020, AJ, 160, 109
Snellen I. A. G., de Kok R. J., de Mooij E. J. W., Albrecht S., 2010, Nature, 465, 1049
Sotzen K. S. et al., 2020, AJ, 159, 5
Sromovsky L. A., Fry P. M., Kim J. H., 2011, Icarus, 215, 292
Stevenson K. B. et al., 2010, Nature, 464, 1161
Tashkun S. A., Perevalov V. I., 2011, J. Quant. Spectrosc. Radiat. Transfer, 112, 1403
Thorngren D., Gao P., Fortney J. J., 2019, ApJ, 884, L6
Tody D., 1993, in Hanisch R. J., Brissenden R. J. V., Barnes J., eds, ASP Conf. Ser. Vol. 52, Astronomical Data Analysis Software and Systems II. Astron. Soc. Pac., San Francisco, p. 173
Tremblin P., Amundsen D. S., Mourier P., Baraffe I., Chabrier G., Drummond B., Homeier D., Venot O., 2015, ApJ, 804, L17
Tremblin P., Amundsen D. S., Chabrier G., Baraffe I., Drummond B., Hinkley S., Mourier P., Venot O., 2016, ApJ, 817, L19
Tremblin P. et al., 2017, ApJ, 841, 30
Tsai S.-M., Lyons J. R., Grosheintz L., Rimmer P. B., Kitzmann D., Heng K., 2017, ApJS, 228, 20
Visscher C., Lodders K., Fegley, Bruce J., 2006, ApJ, 648, 1181
Visscher C., Lodders K., Fegley, Bruce J., 2010, ApJ, 716, 1060
Wakeford H. R., Sing D. K., Evans T., Deming D., Mandell A., 2016, ApJ, 819, 10
Wakeford H. R. et al., 2017a, Science, 356, 628
Wakeford H. R., Visscher C., Lewis N. K., Kataria T., Marley M. S., Fortney J. J., Mand ell A. M., 2017b, MNRAS, 464, 4247
Wakeford H. R. et al., 2018, AJ, 155, 29
Wong M. H., Mahaffy P. R., Atreya S. K., Niemann H. B., Owen T. C., 2004, Icarus, 171, 153
Yurchenko S. N., Amundsen D. S., Tennyson J., Waldmann I. P., 2017, A&A, 605, A95
Žák J., Kabáth P., Boffin H. M. J., Ivanov V. D., Skarka M., 2019, AJ, 158, 120

APPENDIX A: TESS PHOTOMETRY

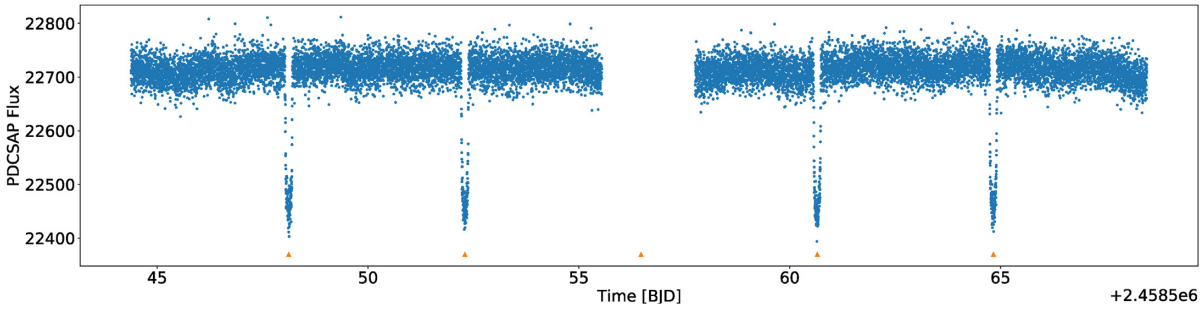

Figure A1. Blue points are *TESS* photometry of WASP-127, orange triangles show expected mid-transit times of WASP-127b.

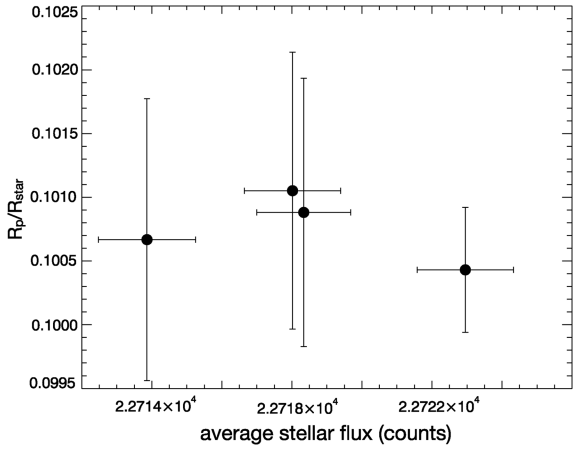

Figure A2. Measured planet-to-star radius ratios from four *TESS* transit events against average stellar flux.

APPENDIX B: LIGHT-CURVE FITTING CORNER PLOTS

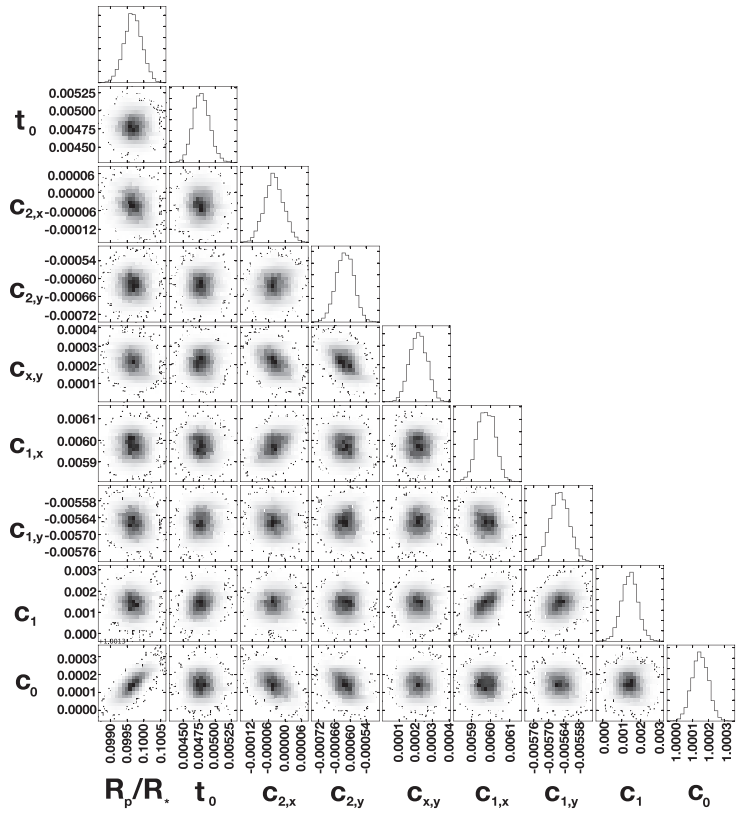

Figure B1. Posterior distributions for light-curve MCMC fits for WASP-127b, using *Spitzer*/IRAC's 3.6 μm channel.

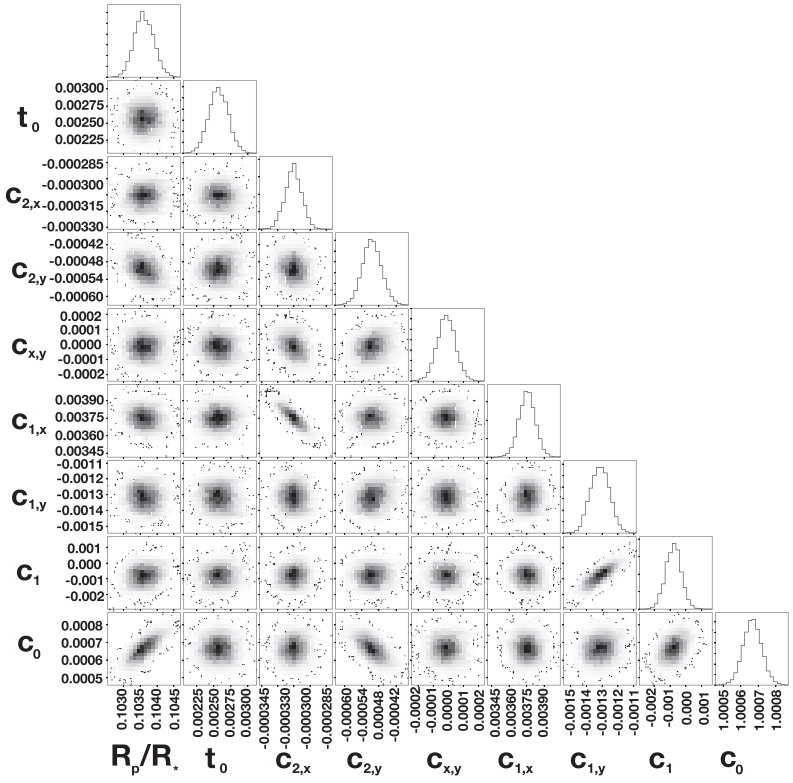

Figure B2. Posterior distributions for light-curve MCMC fits for WASP-127b, using *Spitzer*/IRAC's 4.5 μm channel.

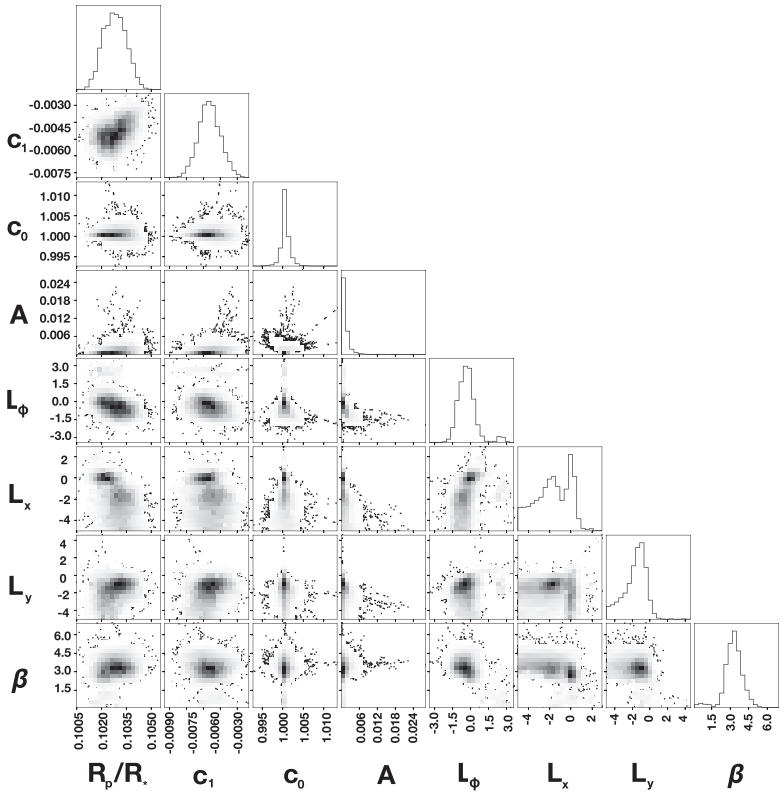

Figure B3. Posterior distributions for white light-curve MCMC fit for WASP-127b, using *HST*/STIS + G430L.

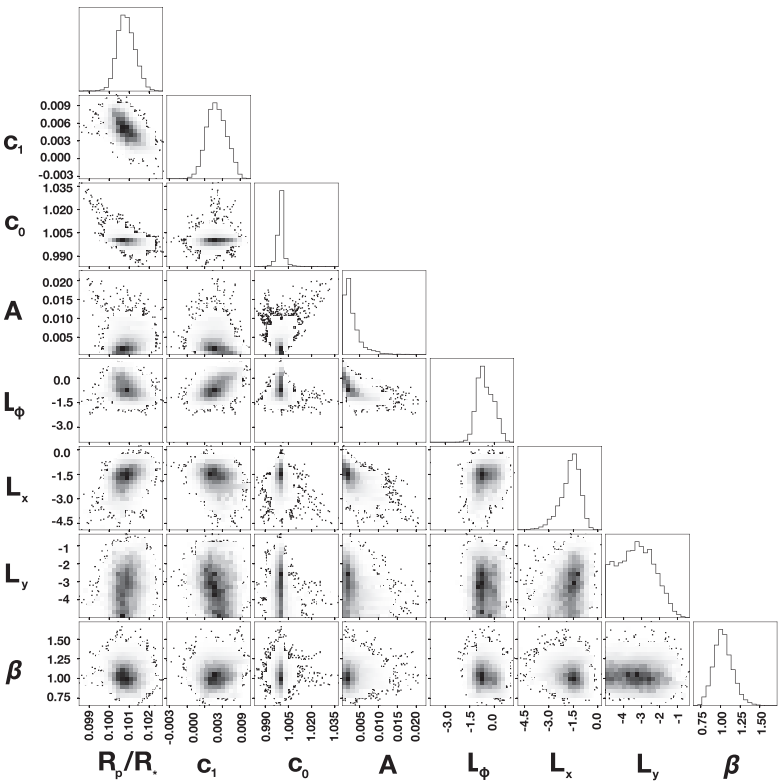

Figure B4. Posterior distributions for white light-curve MCMC fit for WASP-127b, using *HST*/STIS + G750L.

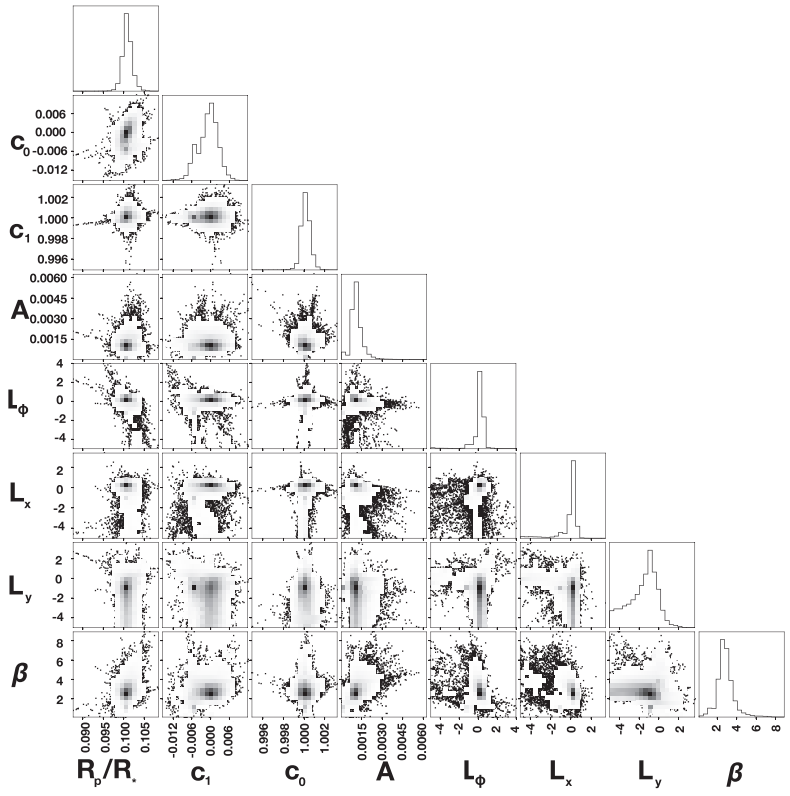

Figure B5. Posterior distributions for white light-curve MCMC fit for WASP-127b, using *HST*/WFC3 + G141.

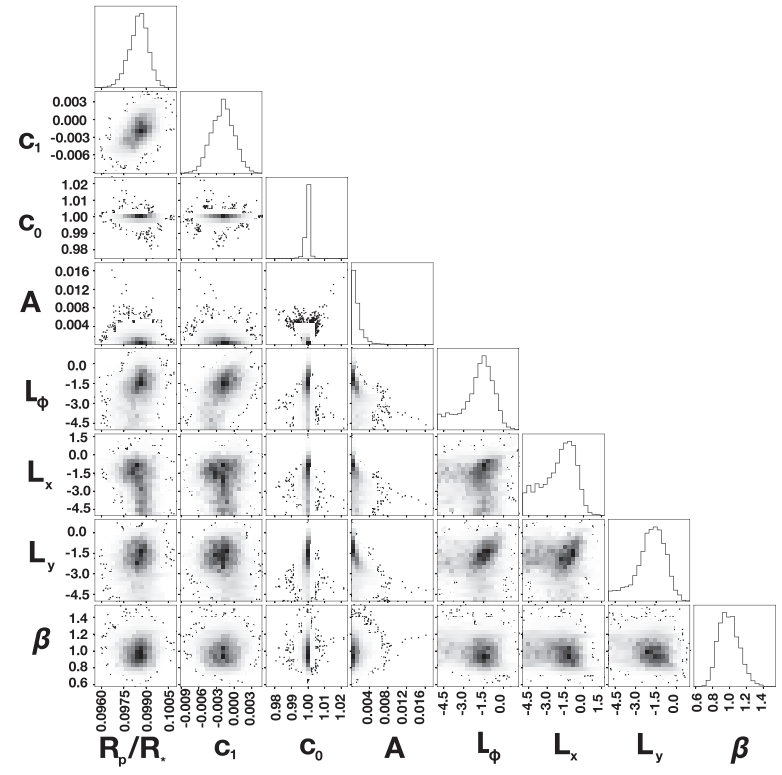

Figure B6. Typical posterior distributions for spectroscopic light-curve MCMC fits for WASP-127b, using *HST*/WFC3 + G141.

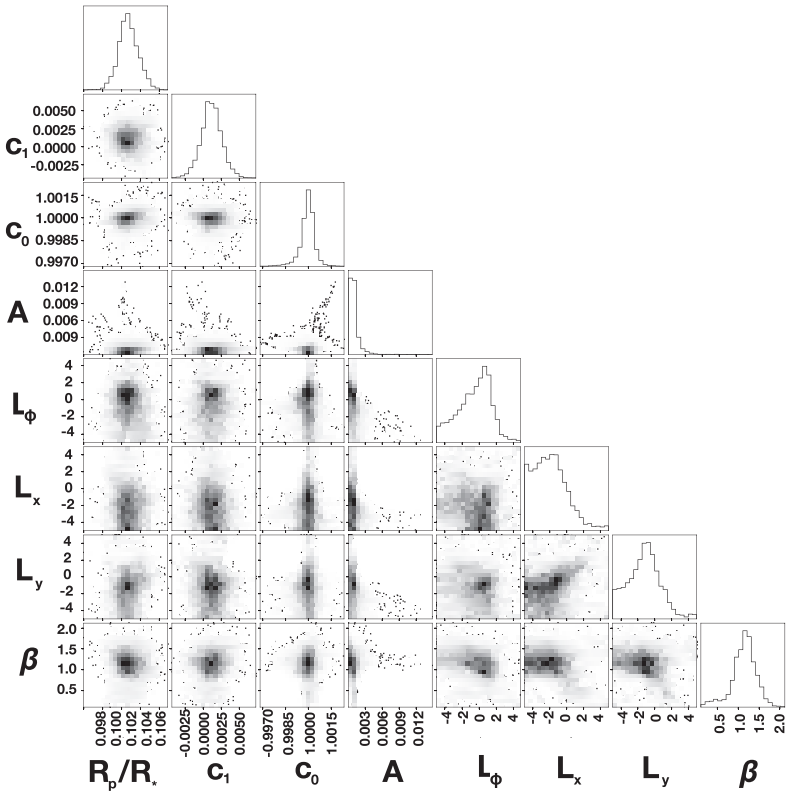

Figure B7. Typical posterior distributions for spectroscopic light-curve MCMC fits for WASP-127b, using *HST*/STIS + G430L.

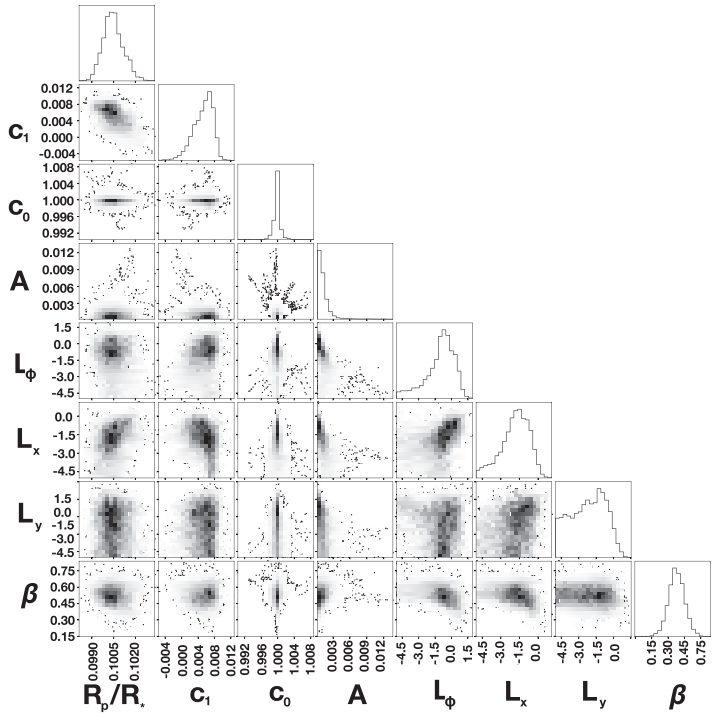

Figure B8. Typical posterior distributions for spectroscopic light-curve MCMC fits for WASP-127b, using *HST*/STIS + G750L.

This paper has been typeset from a TEX/LATEX file prepared by the author.